A genetically defined injured C-fibre nociceptor associated with neuromas drives chronic spontaneous neuropathic pain

Xiangsunze Zeng[1,2], Rosa I. Martinez-Garcia[2,3], Shamsuddin A. Bhuiyan[4], Keunjung Heo[1,2], Natalie MacKinnon-Booth[1], Elke Bentley[1], Emily Shea[1], Kangling Wu[5], Omer Barkai[1,2], Bruna Lenfers Turnes[1,2], Selwyn S. Jayakar[1,2], Barbara Gomez-Eslava[1], Mustafa Q. Hameed[1], Celine Santiago[2,3], Karina Lezgiyeva[2,3], Emmanuella Osei-Asante[2,3], Ivan Furfaro[5], Alexander Rotenberg[1], Benjamin R. Johnston[6], Brian J. Wainger[7,8], William Renthal[4], Stéphanie P. Lacour[5], David D. Ginty[2,3]* & Clifford J. Woolf[1,2]*

[1]F.M. Kirby Neurobiology Center, Boston Children's Hospital, Boston, MA, USA

[2]Department of Neurobiology, Harvard Medical School, Boston, MA, USA

[3]Howard Hughes Medical Institute, Boston, MA, USA

[4]Department of Neurology, Brigham and Women's Hospital, and Harvard Medical School, Boston, MA, USA

[5]Laboratory for Soft Bioelectronic Interfaces (LSBI), Neuro-X Institute, École Polytechnique Fédérale de Lausanne, Geneva, Switzerland

[6]Department of Neurosurgery, Mass General Brigham, and Harvard Medical School, Boston, MA, USA

[7]Department of Anesthesiology, Critical Care and Pain Medicine and Department of Neurology, Massachusetts General Hospital, Harvard Medical School, Boston, MA, USA

[8]Broad Institute of MIT and Harvard, Cambridge, MA, USA

*Corresponding authors. email:

david_ginty@hms.harvard.edu (D.D.G);

clifford.woolf@childrens.harvard.edu (C.J.W.)

Abstract

Spontaneous pain is a common but poorly understood consequence of peripheral nerve injury[1-3], including injuries that lead to the formation of neuromas[4,5]. We developed a chronic neuroma model for measuring spontaneous pain-related behaviours in mice, which revealed that limb flicks - emerging predominantly 2 months post-injury - reflect spontaneous paroxysmal pain. Ectopic activity of injured dorsal root ganglia (DRG) sensory neurons whose axonal endings terminate within the neuroma drives this spontaneous pain. *In vivo* imaging showed that a subset of small-diameter DRG sensory neurons are the source of spontaneous neural signals emanating from the neuroma, and these spontaneously active neurons are distinct from the intact larger diameter sensory neurons that mediate stimulus-evoked mechanical allodynia from spared nerves. Cell-type–specific gain- and loss-of-function studies identified a genetically- and functionally-defined subtype of small-diameter C-fibre nociceptors whose injured axons in neuromas drive spontaneous limb flicks/neuropathic pain. These findings establish the neurobiological basis of spontaneous pain enabling targeted pain management strategies and define a cellular and mechanistic separation between spontaneous and evoked neuropathic pain.

Introduction

Peripheral nerve injury is a major cause of chronic neuropathic pain, resulting in persistent suffering and disability. Spontaneous pain is among the most common and debilitating clinical feature of neuropathic pain[1-3], yet its underlying mechanisms remain largely unknown. Most preclinical research emphasizes stimulus-evoked withdrawal responses[6], which poorly captures the chronic and fluctuating nature of spontaneous neuropathic pain. This knowledge gap stems

from the fact that spontaneous pain arises sporadically and unpredictably, posing challenges for comprehensive quantitative investigations[7] and mechanistic discovery.

Existing measures of spontaneous pain are inadequate. For example, the grimace scale performs well in acute pain settings but not for neuropathic pain[8]. Conditioned place preference can indicate ongoing pain[9], but fails to capture the paroxysmal nature of spontaneous pain—characterized by sudden, episodic bouts—which is a hallmark in patients with peripheral nerve trauma who develop neuromas[10]. Consequently, studies have relied on intermittent pain-like behaviours such as paw biting or guarding to infer spontaneous paroxysmal pain after nerve injury[11,12]. These measures, however, typically depend on short-term video observations and do not provide a comprehensive view of sporadic and unpredictable pain episodes over prolonged periods.

Neuropathic pain research has predominantly centered on acute and subacute post-nerve injury (e.g., 1–4 weeks), leaving its chronic features relatively underexplored[13], even though chronic pain is the major clinical issue. Furthermore, the cellular sources of aberrant activity are unclear: early electrophysiological studies demonstrated that both injured and neighboring uninjured sensory fibres generate ectopic discharges soon after axotomy[12,14,15], but the genetically defined and physiologically distinct sensory subtypes that drive chronic spontaneous neuropathic pain have not been identified. Finally, a longstanding clinical puzzle is why patients with comparable peripheral nerve insults experience different outcomes, with some developing severe chronic pain while others exhibiting moderate or no pain[4,5,16]. Although risk factors, including genetic predisposition, psychosocial context, prior injury, age, and sex, have been proposed[16,17], the cellular and molecular bases for this variability are still elusive.

By integrating long-term home-cage behavioural studies with a novel measure of spontaneous pain, *in vivo* calcium imaging, cell-type–specific optogenetic and chemogenetic manipulations,

70 and transcriptomic profiling in mice, we now identify injured axons of a genetically and
71 functionally defined C-fibre nociceptor subtype as the driver of chronic spontaneous neuropathic
72 pain in animals with painful neuromas. Our findings also reveal a clear cellular and mechanistic
73 distinction between spontaneous and evoked neuropathic pain.
74

75 ## Results

76 **Painful neuromas drive chronic spontaneous pain after peripheral nerve injury**

77 We sought to understand the mechanistic basis of spontaneous neuropathic pain by analysing
78 defined spontaneous behaviours in mice using a machine-learning–based platform[18] following
79 different types of sciatic nerve injury (Extended Data Fig. 1a,b). Guarding, biting/licking,
80 scratching, rearing, and grooming behaviours were monitored using 30-minute recording sessions
81 conducted once per week for up to two months after injury. All of these behaviours remained
82 unchanged post-injury, except for guarding, where mice lift and hold the paw ipsilateral to the
83 nerve injury, which increased relative to sham controls from one week after the injury (Extended
84 Data Fig. 1c), in line with previous studies[11,12].

85 While the conventional behavioural measures did not provide a reliable measurement of
86 spontaneous pain, the long-term videography analysis revealed an unexpected "limb flick"
87 behaviour that was very rare in the first 4 weeks after the nerve injury, but then progressively
88 increased, becoming most prominent at 8 weeks post-injury across all the nerve transection injury
89 models (Extended Data Fig. 1d). This spontaneous limb flick behaviour was characterized as
90 having a stereotyped pattern of rapid, repetitive hindlimb shaking (Supplementary Video 1). The
91 incidence of limb flicks scaled with injury severity, being most pronounced after a full sciatic nerve
92 transection (SNT) and intermediate in the spared nerve injury (SNI) model, where the common

93 peroneal and tibial nerves are injured and the sural nerve remains intact (Extended Data Fig. 1a,d).
94 Limb flicks were also observed after a sural nerve transection (SuNT) (Extended Data Fig. 1a,d),
95 which selectively damages sensory fibres[19], and they were suppressed by gabapentin (Extended
96 Data Fig. 2a), supporting that this behaviour likely reflects pain and not motor dysfunction. By
97 contrast, limb flicks were absent in acute nociceptive or inflammatory pain models (Extended Data
98 Fig. 2b). These observations suggest that spontaneous limb flicks arise from chronic pathological
99 changes in injured sensory nerve fibres.

100 Because the limb flick is a chronic pain-associated behaviour that emerged most robustly in the
101 SNT model, we focused on this nerve injury model for subsequent analyses. To move beyond
102 short-term measures of limb flicks, we established a quantitative framework for long-term home-
103 cage monitoring. Given the stereotyped high-frequency muscle activity underlying limb flicks, we
104 implemented a wireless electromyography (EMG) system using electrodes placed in the vastus
105 lateralis, the largest quadriceps muscle, coupled with video recording, to reliably capture injured
106 hindlimb behaviours over extended time periods (Fig. 1a). The EMG system faithfully detected
107 repetitive limb flick oscillations (Supplementary Video 1), with an average peak frequency of ~13
108 Hz and most events lasting <1 second (Extended Data Fig. 3a–c), without any apparent motor
109 impairment from the recording electrode implantation (Extended Data Fig. 3d). To determine
110 whether prolonged monitoring reduces behaviour variability, we performed continuous 24-hour
111 recording at 8 weeks post-SNT and assessed intra-animal variation by binning the data into time
112 windows of increasing length. As the window size increased, variability progressively declined,
113 and extending the recording period up to 48 hours did not yield a further reduction when compared
114 with 24 hours (Fig. 1b). These results demonstrate that 24-hour monitoring provides a stable

measure of limb flicks and also reveal a circadian component to this spontaneous neuropathic pain behaviour[20].

Using 24-hour recordings, we tracked limb flicks longitudinally. Group averages rose gradually, reaching a peak around 8 weeks post-SNT and remaining at a plateau thereafter, with most increases occurring during the dark phase (7 p.m.–7 a.m.) (Fig. 1c,d). Between mice, the flick prevalence varied, with some mice displaying dramatic increases and others remaining at moderate or low levels throughout the 16-week post-SNT period (Fig. 1d). Unlike the intra-animal variability attributable to recording length, this inter-animal variability likely reflects biological differences and is reminiscent of the different pain phenotypes in patients who develop painful or non-painful neuromas after peripheral nerve injury or an amputation[4,5]. Histology confirmed the formation of terminal neuromas proximal to the nerve transection, appearing as bulbous structures filled with exuberant but disorganized axons within fibrotic tissue by 8 weeks post-SNT (Fig. 1e), as described previously[21]. To test whether the neuromas trigger the limb flicks, we used a transcutaneous poke test, analogous to the clinical Tinel sign evoked by gentle tapping the skin over a peripheral nerve[22]. Our poke test involved indenting the skin overlying the SNT lesion with a 15 g von Frey filament to mechanically stimulate the underlying neuroma (hereafter referred to as "transcutaneous neuroma poke"). This stimulus increasingly induced limb flicks over time across the nerve injury models, with the strongest responses in SNT animals, and minimal responses in sham controls or when applied to the side contralateral to the SNT surgery (Extended Data Fig. 4a and Supplementary Video 2). EMG implantation did not affect this outcome (Extended Data Fig. 3e). We also assessed flick probability to the transcutaneous neuroma poke in the same mice that were used for the 24-hour spontaneous flick recordings. This analysis revealed comparable inter-animal variability as spontaneous limb flicks (Fig. 1f) and also demonstrated a

138 strong positive correlation in the chronic phase: mice with more spontaneous limb flicks were also
139 highly sensitive to the poke test, whereas those with few spontaneous limb flicks showed little or
140 no flick response to a poke (Fig. 1g). To test causality, we injected lidocaine locally at the neuroma
141 site, a standard clinical intervention[23]. This virtually abolished the poke-induced flicks in mice
142 with a high neuroma pain behaviour. In addition, lidocaine treatment markedly reduced
143 spontaneous flicks (Fig. 1h), indicating that activity originating in neuromas is the major driver of
144 this chronic spontaneous pain behaviour.

145 To quantify the incidence of the high-pain phenotype, we performed the transcutaneous
146 neuroma poke test in 144 mice at 8–12 weeks post-SNT. Thirty-two percent of SNT mice exhibited
147 a high response probability (≥0.7; hereafter referred to as high-pain), twenty-seven percent
148 exhibited low probability (≤0.3; low-pain), and forty-one percent displayed an intermediate pain
149 phenotype (0.4–0.6; medium-pain), with no sex differences or correlation with the neuroma size
150 (Extended Data Fig. 4b,c). Finally, neither poke-induced nor spontaneous limb flicks required the
151 mechanosensitive channel Piezo2, as evaluated in Piezo2 conditional knockout mice (Extended
152 Data Fig. 5).

153

154 **Injured small-diameter sensory axons exhibit ectopic activity arising from their terminals in**
155 **the neuroma**

156 To investigate the neuronal basis of the spontaneous pain, we performed *in vivo* calcium imaging
157 from the L4 dorsal root ganglia (DRG) 8–12 weeks after SNT using *Vglut2*^{Cre}*::GCaMP6f* mice, in
158 which primary DRG sensory neurons across all subtypes are labelled. The neuroma or contralateral
159 intact nerve was surgically exposed to allow direct stimulation with von Frey filaments of varying
160 force (Fig. 2a). Poking neuromas induced calcium responses almost exclusively in small-diameter

161 neurons (<25 μm soma diameter), whereas stimulation of the contralateral intact nerve rarely
162 activated neurons of any size, with the 1.4 g filament producing the most discriminating response
163 (largest effect size determined by Cohen's d) (Fig. 2b,c). Neuroma-poke responses also varied
164 across animals: the response amplitude of small-diameter neurons induced by the 1.4 g probe
165 stimulus differed substantially across mice and was positively correlated with their behavioural
166 pain responsiveness, assessed by transcutaneous neuroma poke immediately prior to the imaging
167 (Fig. 2d), supporting a peripheral contribution to the differential pain outcomes in individual mice.
168 We next assessed spontaneous activity in the same DRG and found that the L4 DRG ipsilateral
169 to the neuroma contained more spontaneously active cells than the contralateral L4 DRG
170 containing neurons with an intact sciatic nerve, specifically within the small-diameter population
171 (Fig. 2e). Comparing the ipsilateral spontaneously active neurons with those responsive to a
172 neuroma poke showed that the majority—both spontaneously active and those responsive to a
173 poke—were small-diameter neurons (Fig. 2f,g). Moreover, topical lidocaine applied directly at the
174 neuroma largely abolished the spontaneous activity (Fig. 2h), demonstrating that the origin of this
175 spontaneous neural activity is in the neuroma rather than the DRG. These findings establish injured
176 small-diameter sensory axons as the principal source of ectopic activity and the likely drivers of
177 spontaneous neuropathic pain.
178
179 **Pain arising from injured versus uninjured fibres requires distinct sensory neuron cell types**
180 Peripheral nerve injury induces ectopic activity in both injured and adjacent uninjured fibres across
181 different sensory neuron subtypes[12,14,24,25]. We next asked whether activity originating from injured
182 fibres in neuromas and uninjured fibres jointly contribute to a common pain phenotype or act
183 through distinct mechanisms. Because the entire sciatic nerve is severed in the SNT model, we

184 assessed mechanosensitivity of the medial plantar paw which is innervated by the intact saphenous
185 nerve [26]. Tactile allodynia associated with the medial plantar paw emerged 4 weeks post-SNT (Fig.
186 3a), well before spontaneous limb flicks became prevalent. No correlation was found between the
187 intact saphenous nerve-evoked pain and neuroma pain intensity (Fig. 3b), pointing to independent
188 mechanisms. Direct imaging of DRG activity confirmed this separation: completely distinct
189 populations of sensory neurons were engaged in the two pain models. Medium- and large-diameter
190 DRG neurons were the primary responders to medial plantar stimulation, whereas small-diameter
191 neurons were predominately associated with neuroma stimulation (Fig. 3c–f; and Supplementary
192 Video 3). Locally silencing the neuroma or saphenous nerve endings with lidocaine selectively
193 inhibited responses initiated from each region, respectively (Fig. 3g,h), providing evidence that
194 pain arising from injured and uninjured fibres is initiated through distinct mechanisms.
195

196 **A genetically defined subtype of C-nociceptor axons in neuromas drives limb flicks**

197 Transcriptomic studies have identified at least 16 genetically distinct DRG sensory subtypes[27-31]
198 with unique physiology and morphology[28]. We performed single-nucleus RNA sequencing
199 (snRNA-seq) of DRG from mice 10 weeks post-SNT and confirmed the presence of all these cell
200 types in both high- and low-pain conditions (Fig. 4a and Extended Data Fig. 6a). To identify
201 specific sensory subtypes whose activation may drive spontaneous limb flicks, we conducted an
202 optogenetic gain-of-function screen, using transgenic mouse lines that collectively encompass the
203 majority of sensory subtypes with soma diameters <25 μm [28]. Because neuromas reside deep
204 within fibrotic tissue, we adapted a miniaturized LED cuff [32] for localized epineural activation of
205 sensory axons, either in neuromas or contralateral intact nerves (Fig. 4b and Extended Data Fig.
206 7). In mice expressing opsins in a subset of small-diameter C-fibres marked by *Sstr2* expression

207 (SSTR2; *Sstr2*$^{T2a\text{-}CreER}$;*Calca-FlpE;R26*$^{LSL\text{-}FSF\text{-}ReaChR::mCitrine}$), a single 10-ms 470-nm pulse
208 delivered to the neuroma induced limb flicks and, to a lesser extent, other pain-related behaviours
209 (vocalization, jump, licking, and avoidance, either individually or in combination)[7], with
210 significantly lower activation thresholds than those needed to evoke behavioural responses on the
211 contralateral intact nerve (Fig. 4c,d). The nomenclature for this cell type varies across the literature,
212 depending on the response modality assessed in intact tissue: C-Heat thermonociceptor (C-Heat
213 [SSTR2]) from skin[28]; C-high threshold mechanoreceptors (C-HTMR) from colon[33], lineage
214 subtype (CGRP-α)[29], marker gene expression in mice (*Calca* + *Sstr2*)[30], hierarchical
215 transcriptomic clustering within the peptidergic branch (PEP1.1) [31], and putative human
216 homologues (C-PEP.TAC1/CACNG5)[34]. Here, we refer to this genetically defined, neuroma-
217 hypersensitive C-fibre subtype as 'Neuroma C-Nociceptors (SSTR2)'. In contrast, Aδ-
218 HTMR/Heat (SMR2) neurons, which are myelinated mechanonociceptors[35], elicited behavioural
219 responses when intact nerves were stimulated but rarely when neuromas were activated (Fig. 4c,d).
220 This discrepancy likely reflects the preferential loss of the axons of these Aδ-HTMR/Heat (SMR2)
221 neurons in neuromas (Extended Data Fig. 8). Other subtypes showed little or no nocifensive
222 behavioural responses when activated: activating Aδ-low-threshold mechanoreceptors (Aδ-
223 LTMRs), C-LTMRs, and C-HTMR/Heat (CYSLTR2/SST) neurons elicited no consistent
224 behaviours from either neuromas or intact nerves, whereas stimulating C-HTMR/Heat
225 (MRGPRA3), C-HTMR/Heat (MRGPRB4), C-HTMR/Heat (MRGPRD), C-Cold (TRPM8) axons
226 with strong optical power occasionally evoked avoidance, guarding, or licking behaviours from
227 either site, but rarely induced limb flicks (Fig. 4c,d; and Supplementary Video 4).
228 Anatomical analyses revealed denser Neuroma C-Nociceptor (SSTR2) fibres in neuromas than
229 in contralateral intact nerves, but a reduced presence of Aδ-HTMR/Heat (SMR2), C-HTMR/Heat

230 (MRGPRA3), and C-HTMR/Heat (MRGPRD) nerve fibres, with C-HTMR/Heat (MRGPRD)
231 axons almost completely absent (Extended Data Fig. 8), likely reflecting cell death in this
232 population after peripheral nerve trauma[36].

233 Because activation of the Neuroma C-Nociceptor (SSTR2) injured axons robustly induced limb
234 flicks, we further characterized how their activity relates to different pain-related behaviours and
235 response dynamics. High-frequency or prolonged optogenetic stimulation did not change the
236 incidence of limb flicks or most other behaviours, except audible vocalizing - a response uniquely
237 triggered by activation of the Neuroma C-Nociceptors (SSTR2) - showed an increased occurrence
238 under these stimulation patterns, suggesting a dependence on summation of activity (Extended
239 Data Fig. 9a). Response latency analyses showed that the limb flicks occurred with an average
240 latency of 259 ms, which was longer than the latency to jump or avoid the stimulus but
241 considerably shorter than the latency for self-licking (Fig. 4e, left). These temporal distinctions
242 suggest that limb flicks represent a pain-related behavioural output that is dissociable from rapid
243 withdrawal reflexes[35] and from delayed coping behaviours. Lastly, we noted from the snRNA-seq
244 analysis that *Scn10a* (encoding voltage-gated sodium channel $Na_v1.8$) and *Scn3a* ($Na_v1.3$) were
245 selectively upregulated in Neuroma C-Nociceptors (SSTR2) under high-pain conditions (Extended
246 Data Fig. 6b,c), potentially linking these ion channels to hyperexcitability of this population in
247 painful neuromas. Related to this, we analysed the optical stimulation strength required to induce
248 limb flicks in high-, medium-, and low-pain mice. We used a Cox proportional hazards model with
249 optical power as the ordered exposure variable and the first limb flick to optogenetic stimulation
250 as the event. This analysis revealed that the flick probability determined by the transcutaneous
251 neuroma poke test significantly predicted optogenetic threshold (*hazard ratio = 198.8*, $p = 0.0023$);
252 high-pain mice flick at a lower optical power, whereas low-pain mice require a higher optical

253 power to elicit flicks (Fig. 4e, right). This result is consistent with increased excitability of
254 Neuroma C-Nociceptors (SSTR2) in high-pain neuromas potentially mediated by upregulation of
255 voltage-gated sodium channels[24].

256 We next asked whether activity of the Neuroma C-Nociceptors (SSTR2) is necessary for
257 neuroma-driven pain behaviours. We acutely silenced this neuronal population using
258 chemogenetic inhibition highly specific to the *Sstr2*$^{+}$ population (*Sstr2*$^{T2a\text{-}CreER}$;*R26*$^{LSL\text{-}hM4Di::mCitrine}$)
259 (Extended Data Fig. 9b). This manipulation significantly suppressed transcutaneous
260 neuroma poke–induced limb flicks in high-pain mice but not in littermate controls (Fig. 4f).
261 Notably, motor function and mechanical allodynia arising from the intact saphenous nerve-
262 innervated area were unaffected (Fig. 4f and Extended Data Fig. 9c), indicating a specific role for
263 activity in injured Neuroma C-Nociceptors (SSTR2) in driving pain arising from the neuroma.
264 These findings define a specific nociceptor subtype whose injured axons become hypersensitive
265 in painful neuromas to drive a chronic spontaneous pain-related behaviour.

266

267 **Discussion**

268 The mechanisms of spontaneous neuropathic pain are obscure, largely because of the lack of
269 reliable measures, particularly over chronic timescales. Most mechanistic insights into neuropathic
270 pain have been derived from stimulus-evoked pain arising from uninjured afferents[26], potentially
271 biasing interpretation toward spared-nerve pathways after injury. By establishing a long-term
272 recording platform, we identified limb flicks as a robust behavioural readout of chronic
273 paroxysmal spontaneous pain and traced their origin to injured axons of a genetically defined
274 sensory subtype within painful neuromas. These findings support the conclusion that the
275 spontaneous and evoked components of neuropathic pain arise from distinct peripheral drivers.

This distinction reframes prevailing models of neuropathic pain and has direct implications for treatment. Prior work indicates that mechanical allodynia mediated by spared nerves after injury is primarily initiated by Aδ/Aβ-LTMRs whose central afferents reroute into nociceptive circuits through dorsal horn plasticity[37,38], with Piezo2-dependent mechanotransduction playing a central role[39]. By contrast, our model identifies injured Neuroma C-Nociceptors (SSTR2) as the principal drivers of neuropathic pain, and with neuroma mechanical hypersensitivity occurring independently of Piezo2 (Extended Data Fig. 5), which is consistent with minimal expression of Piezo2 in this neuronal subtype[28-31]. Defining the pain transduction mechanisms at neuroma terminals[24], and how Neuroma C-Nociceptors (SSTR2) engage central circuits to generate pain perception, will advance our understanding of the underlying mechanisms of spontaneous neuropathic pain.

Consistent with the mechanistic separation of spontaneous and evoked pain, both preclinical and clinical evidence suggests that spontaneous pain and stimulus-evoked hypersensitivity are distinct in their pharmacological responsiveness[40-43]. However, current diagnostic frameworks lump these manifestations under a single "neuropathic pain" label, and treatment guidelines recommend single agents without any delineation for evoked or spontaneous pain. This likely contributes to variable therapeutic efficacy through a mechanism–therapy mismatch. Our findings support the need to revisit diagnostic criteria to explicitly distinguish between spared-fibre evoked allodynia and injured-fibre triggered spontaneous pain, and develop specific targeted interventions aligned with the dominant mechanistic driver in individual patients.

A second key implication is that identifying the peripheral driver of spontaneous pain provides a rational framework for cell-targeted intervention[44]. Because Neuroma C-Nociceptors (SSTR2) are both necessary and sufficient to drive neuroma pain, and their selective silencing suppresses

299 neuroma pain without impairing sensory modalities from spared nerves or motor function (Fig. 4f
300 and Extended Data Fig. 9c), therapeutic strategies that act selectively within this population,
301 particularly those enabling localized, subtype-specific delivery[45], offer a means to alleviate
302 pathological pain while preserving desired sensory function and minimizing central exposure in
303 patients. Although the Neuroma C-Nociceptors (SSTR2) identified here are defined by *Sstr2*
304 expression in mice—a marker with minimal expression in human DRG neurons—the model
305 recapitulates key clinical features of neuropathic pain, suggesting the existence of an evolutionarily
306 conserved homologous human nociceptor subtype, which is supported by transcriptomic
307 observations[34]. Defining the analogous mechanisms operating in humans and identifying
308 molecular access points to suppress neuroma-associated hyperexcitability will be essential for
309 translation.

310 Beyond symptomatic control, preventing the formation of painful neuromas may be a new
311 treatment strategy. The emergence of high-pain versus low-pain phenotypes that can be decoded
312 at the level of sensory neuron activity (Fig. 2d) points to peripheral heterogeneity in how neuromas
313 are primed after injury. Such variability may reflect differences in stochastic perturbations of gene
314 expression during the early injury response[46,47], local trophic and inflammatory signaling[48], and
315 interactions with diverse non-neuronal cell types[48-52]. Defining the determinants that govern
316 painful neuroma maturation during the subacute formation phase may therefore enable early
317 protective strategies that can intercept pathological trajectories before chronic spontaneous pain
318 becomes established, enabling its prevention[44].

319 # Methods

320 **Mice**

321 All experiments were conducted in accordance with the guidelines of the Boston Children's
322 Hospital Institutional Animal Care and Use Committee (IACUC) under protocols 00001507 and
323 00002403, or by the Harvard Medical School IACUC under protocol IS00001036-9. Mice were
324 housed under temperature-controlled conditions on a 12-hour light/dark cycle (lights on at 7:00
325 a.m., off at 7:00 p.m.) with ad libitum access to food and water. Both male and female mice were
326 used in all experiments. The C57BL/6J strain (JAX #000664; The Jackson Laboratory) was used
327 unless otherwise specified, with transgenic strains detailed in the relevant sections below.

328

329 **Peripheral nerve injury models**

330 Surgeries were performed on 8–9-week-old mice under aseptic conditions. Anaesthesia was
331 induced and maintained with 2% isoflurane (Patterson Veterinary, #07-890-8115) delivered via a
332 nose cone. Throughout the procedure, body temperature was maintained at 37°C using a heated
333 pad to prevent hypothermia. Sciatic nerve injuries were performed using standardized protocols as
334 follows. 1. The surgical site was shaved, and residual hair was completely removed using Nair.
335 The area was then sterilized with 70% ethanol and Betadine. 2. A small skin incision was made
336 over the lateral thigh, above the biceps femoris. The underlying musculature was carefully
337 separated and retracted to expose the sciatic nerve. 3. For sham controls, the sciatic nerve was
338 gently freed from surrounding connective tissue using curved forceps without causing any damage.
339 For SNT injury, a segment of the sciatic nerve trunk 5 mm above the sural, common peroneal, and
340 tibial nerves was ligated with 6-0 sutures (Ethicon, #K889H) followed by a complete transection
341 proximal to the ligation using microsurgical scissors. An additional 5 mm segment of the distal

342 nerve stump was excised. For SNI injury, the common peroneal and tibial nerve branches were
343 ligated and transected in the same manner, leaving the sural nerve intact. For SuNT injury, the
344 sural nerve branch was ligated and transected in the same manner, leaving the common peroneal
345 and tibial nerve branches intact (Extended Data Fig. 1a). 4. The musculature was then folded back
346 to cover the sciatic nerve with the skin closed with 6-0 sutures. 5. Mice were placed on a 37°C
347 heated pad postoperatively until they fully recovered before being returned to their home cages.
348

349 **Automated behavioural screening**

350 The recording setup and analytic platform were identical to those previously described[18]. Briefly,
351 mice were recorded inside a black acrylic enclosure (18 × 18 × 15 cm; length × width × height),
352 which was closed on all sides except for the bottom and positioned on a 25-cm square piece of 5-
353 mm thick glass floor. To ensure consistent illumination from below, two independent 850-nm near-
354 infrared (NIR) LED strips (SMD5050-300-IR, Huake Light Electronics Co., Ltd., Shenzhen,
355 China) were mounted 10 cm beneath the glass floor. These were carefully positioned to prevent
356 reflections from interfering with the recorded images. The LED strips were powered by a 12-V
357 DC power supply. Video recordings were acquired in darkness using an NIR camera (Basler
358 acA2000-50gmNIR GigE, Basler AG, Ahrensburg, Germany) positioned 30 cm below the glass
359 surface. Pylon viewer software (v4.1.0.3660, Basler) was used to capture videos under
360 standardized camera settings. All recordings were conducted at 25 Hz with an initial resolution of
361 1000 × 1000 pixels, which was subsequently downsized to 500 × 500 pixels for high throughput
362 analysis. For each injury type, four male and four female C57BL/6J mice were used. To minimize
363 stress and ensure natural behaviour, mice were habituated for 30 minutes in the recording chamber

364 followed by a 30-minute recording session at each time point (Extended Data Fig. 1c,d). Only one
365 mouse was placed in the chamber at a time.
366 To analyse behaviours from the recordings, we used BAREfoot, a supervised machine learning
367 algorithm that integrates pose estimation with light-based measurements of body-part pressure and
368 distance[18]. For behaviours without pre-existing classifiers, training datasets were generated by
369 manual annotation of videos by experienced scorers, and new classifiers were subsequently trained.
370 The resulting library of trained classifiers enabled automated, frame-by-frame scoring of a
371 behavioural repertoire that included spontaneous rearing, grooming, scratching, biting/licking,
372 guarding, and limb flicks in freely moving mice.
373
374 **Home-cage EMG/video recording system**
375 Implantation of wireless telemetry transmitters and recording was performed aseptically in 8-
376 week-old C57BL/6J mice under 2% inhaled isoflurane anaesthesia. Wireless telemetry transmitters
377 (PhysioTel ETA-F10; Data Sciences International, St. Paul, MN) were implanted by making a short
378 skin incision along the dorsal aspect of the left hindlimb. A subcutaneous pocket was created by
379 blunt dissection over the back, cephalad to the hindlimb, to house the transmitter body. For EMG
380 recording, a pair of recording and reference electrode leads were stripped of silicone insulation
381 over a 2–3 mm segment, inserted into the vastus lateralis muscle, and secured to the muscle surface
382 with 5-0 nylon sutures to prevent displacement. The incision was closed with surgical staples and
383 tissue adhesive, and mice were returned to their home cages to recover for ~2 weeks before
384 undergoing the SNT procedure. For experiments shown in Fig. 1d,f, sham controls included 3
385 males and 2 females, and the SNT group included 6 males and 4 females. Mice in the sham group
386 were also used to assess weight bearing and gait parameters post-implantation (Extended Data Fig.
387 3d) using a previously reported behavioural platform [53]. In a separate cohort, 3 high-pain and 3

388 low-pain mice at 8 weeks post-SNT were implanted with transmitters to evaluate the impact of
389 implantation on neuroma pain sensitivity (Extended Data Fig. 3e).

390 Mice were housed in custom-designed home cages equipped with overhead video cameras with
391 night-vision, maintained under a 12-hour light/12-hour dark cycle (lights on at 7 a.m. and off at 7
392 p.m.) in temperature- and humidity-controlled chambers, with ad libitum access to food and water
393 (Fig. 1a). In a subset of animals, four additional side-view IP cameras (M1145-L Network Camera,
394 Axis) were used. Video/EMG recordings (sampled at 1000 Hz) were acquired in real time using
395 the DSI Ponemah data acquisition platform (Data Sciences International, St. Paul, MN).

396 To examine the frequency-domain characteristics of EMG signals representing different
397 behaviours, we performed fast Fourier transform (FFT) analysis on raw EMG time series data with
398 Python's scipy.fft module to determine dominant frequency for each behaviour defined by video
399 observations (Extended Data Fig. 3a). The raw amplitude values of the corresponding time series
400 were first transformed into the frequency domain. The resulting spectrum was computed over the
401 range of 0 to 200 Hz. To facilitate comparison across time series and to highlight relative peak
402 frequencies independent of absolute amplitude differences, the FFT magnitude spectrum for each
403 trace was normalized by dividing all frequency amplitudes by the maximum amplitude within that
404 trace. This rescaled the values to a range between 0 and 1, allowing identification of the dominant
405 frequency peaks while minimizing inter-sample variability in absolute signal strength (Extended
406 Data Fig. 3c, right). Event amplitudes were defined as the absolute peak-to-peak value during each
407 event (Extended Data Fig. 3b). Autocorrelation was computed using the autocorrelation function
408 up to 1000 ms using FFT-based methods. The first positive peak after lag 0 was identified to extract
409 both the dominant periodicity and its autocorrelation strength (Extended Data Fig. 3b).

410 For scoring limb flicks, raw EMG signals were bandpass filtered at 5–30 Hz. Limb flicks were
411 defined as bouts of repetitive spikes in the filtered EMG trace (Fig. 1a and Supplementary Video
412 1). Based on features distinguishing limb flicks from other behaviours (Extended Data Fig. 3a,b),
413 we implemented a two-step semi-manual scoring pipeline. First, EMG traces were screened using
414 a dynamic threshold–based automated spike detection algorithm in NeuroScore CNS Data
415 Analysis Software (v3.6; DSI, Data Sciences International, St. Paul, MN) with broad parameters
416 as follows. Threshold ratio: 1.2; Maximum ratio: 3; Minimum value: 5 μV; minimum spike
417 duration: 1 ms; Maximum spike duration: 1000 ms; Minimum inter-spike interval: 10 ms;
418 Maximum inter-spike interval: 1000 ms; Minimum spike train duration: 10 ms; and Minimum
419 number of spikes: 2. This automated step detected >95% of true-positive events as confirmed in
420 pilot observations. Second, automatically detected events were reviewed by an experimenter
421 blinded to the experimental condition (sham vs. SNT and time point post-surgery), who cross-
422 referenced detection timestamps with simultaneous video recordings to exclude false positives.
423 The coefficient of variation was calculated as the standard deviation divided by the mean of flick
424 counts within each binned time window. Ten 24-hour recordings of SNT mice were randomly
425 selected to compute variation across bin sizes ranging from 0.5 to 12 hours. A subset of five mice
426 was recorded for 6 consecutive days to compute CV across extended 12-, 24-, and 48-hour
427 windows (Fig. 1b).
428
429 **Transcutaneous neuroma poke test**
430 Mice were shaved around the thigh area before behavioural assay. Acclimation was conducted over
431 two consecutive days prior to the actual test. During acclimation, mice were placed on a laboratory
432 bench while the investigator gently held their tails. A series of pokes (20–50 repetitive trials

433 covering the entire thigh area, ~15 minutes per mouse) were applied using a 15 g von Frey filament
434 (Stoelting Co, #58011) to familiarize the animals with the testing environment. This acclimation
435 step was crucial, as mice otherwise exhibited escaping behaviour in response to mechanical
436 stimulation, even in the absence of injury. Following acclimation, mice typically remained calm
437 and stationary, indicating readiness for the actual behavioural test (Supplementary Video 2). If
438 mice continued to display escaping or excessive movements, acclimation was extended until they
439 reached a stable state. Additionally, trials during this acclimation process enabled the investigators
440 to identify a 'target point'—the area on the thigh that elicited the most consistent flicking response.
441 This point often corresponded to the precise location of the neuroma, as later confirmed by *post-*
442 *hoc* dissection. In mice that did not exhibit a flicking response throughout acclimation, the 'target
443 point' was set on the skin area directly above the site of the nerve transection.
444 For the behavioural test, 10 trials of mechanical stimulation were applied to the identified 'target
445 point' using the 15 g von Frey filament, with an inter-stimulus interval of >5 seconds. If a stimulus
446 did not evoke an immediate flicking response, it was maintained for 3 seconds. Trials with no
447 response after this duration were counted as non-responsive (Supplementary Video 2). Since
448 injured mice sporadically exhibited spontaneous flicking behaviours, any response occurring more
449 than 2 seconds after stimulus offset was not counted, and the trial was repeated. Occasionally, mice
450 exhibited other behaviours to pokes (e.g., licking or guarding), which were not quantified as they
451 were rare and also occurred on the contralateral side. Flicking probability to poke was quantified
452 as the proportion of trials that elicited flicking behaviours relative to the total number of trials. For
453 animals tested repeatedly on different days, investigators were blinded to their previously assessed
454 pain phenotype.
455

456 **Plantar von Frey assay**

457 Mice were placed individually in transparent plastic chambers on a wire mesh grid and acclimated
458 to the testing environment for 60 minutes on two consecutive days. Calibrated von Frey filaments
459 (0.008–4.0 g) were applied to the medial plantar surface (saphenous nerve territory) of the injured
460 side using the Up-Down method[54]. Testing was performed 1 day before SNT and weekly thereafter
461 up to 8 weeks post-SNT, and 50% withdrawal thresholds were calculated (Fig. 3a).

462 For plantar von Frey testing in Piezo2 conditional knockout mice generated from *Cdx2*^{Cre} (JAX
463 #009350)[55], *Piezo2*^{flox} (JAX #027720) and *Piezo2*$^{flox/Null}$ strains[56], the contralateral central plantar
464 area was targeted using the same Up-Down method (Extended Data Fig. 5).

465

466 **Drug treatments and chemogenetic silencing experiments**

467 For the drug-related tests, spontaneous behavioural assessments were performed in the black box
468 recording system (Extended Data Fig. 1b) for 30 minutes rather than in the home-cage monitoring
469 setup, as the effective window of drug action is on the scale of hours. To mitigate intra-animal
470 variability and ensure robust statistical power, a larger sample size was included. Gabapentin
471 (Medisca, #60142-96-3) was administered intraperitoneally at 30 mg/kg. Spontaneous behaviours
472 were recorded in the black box for 30 minutes before injection (pre) and again for 30–60 minutes
473 post-injection (Extended Data Fig. 2a). Compound 21 (Hello Bio, #HB4888) was administered
474 intraperitoneally at 3 mg/kg to mice carrying either the hM4Di allele (B6.129-
475 *Gt(ROSA)26Sor*$^{tm1(CAG-CHRM4,-mCitrine)Ute}$/J; JAX #026219) alone, *Sstr2*$^{T2a-CreER}$ alone, or hM4Di
476 under the control of *Sstr2*$^{T2a-CreER}$. Transcutaneous neuroma poke tests were conducted 40–50
477 minutes post-injection (Fig. 4f). 50 µl 1% lidocaine hydrochloride monohydrate (Sigma-Aldrich,
478 #L5647) was administered via deep intramuscular–perineural injection around the lateral upper

479 thigh where the neuroma resides. Spontaneous behaviours were recorded for 30 minutes beginning
480 15 minutes after injection, immediately followed by transcutaneous neuroma poke tests conducted
481 45–55 minutes post-injection (Fig. 1h). For calcium imaging experiments, 10 μL of 1% lidocaine
482 hydrochloride monohydrate was applied either topically to surgically exposed neuromas (Fig. 2h
483 and Fig. 3g) or via intraplantar injection (Fig. 3h), and von Frey assessments were performed 5
484 minutes after administration. Capsaicin (Sigma-Aldrich, #M2028), zymosan (Sigma-Aldrich,
485 #Z4250), and CFA (Sigma-Aldrich, #F5881) were administered as described in the legend to
486 Extended Data Fig. 2b. Spontaneous limb flicks and paw biting/licking behaviours were manually
487 counted by investigators blinded to the treatments.
488
489 ***In vivo* imaging of DRG activity**
490 DRG imaging was performed as described previously[38]. Mice carrying both *Vglut2-ires-Cre*
491 (B6J.129S6(FVB)-*Slc17a6*$^{tm2(cre)Lowl}$/MwarJ; JAX #28863) and *Ai95D* (B6J.Cg-
492 *Gt(ROSA)26Sor*$^{tm95.1(CAG-GCaMP6f)Hze}$/MwarJ; JAX #028865) alleles were used for imaging at 8–12
493 weeks post-SNT. Anaesthesia was induced with 2.5% isoflurane and maintained at 2% via a nose
494 cone. Mice were placed on a heated pad to maintain the body temperature at 37 °C, and ophthalmic
495 ointment was applied to the eyes throughout the surgery and imaging. The back was shaved, and
496 a rectangular incision was made between the lumbar enlargement and pelvic bone with the skin
497 folded away. A dorsal laminectomy was performed in four steps. First, a 1.5-cm midline incision
498 caudal to the lumbar enlargement area was made to create space for clamping. Second, a 3–4 mm
499 incision was made approximately 1 cm rostral to the pelvic bone to expose the spine where the L4
500 DRG is situated. Third, muscles and connective tissues were removed with scissors and forceps.
501 Fourth, the L4 transverse process was excised using rongeurs, and small vertebral fragments were

502 carefully trimmed with fine forceps to fully expose the DRG. Bleeding was controlled using
503 absorbent paper points (Electron Microscopy Sciences, #71011-01). To minimize motion artifacts
504 from respiration, a custom spinal clamp was used to secure the spine over the vertebrae 5 mm
505 rostral to the L4 DRG. Illumination was provided with a collimated 470 nm light-emitting diode
506 through a 10x, 0.3 numerical aperture air objective. The clamp was adjusted to ensure the DRG
507 surface was as level as possible, visualizing the maximum surface area in the focal plane, typically
508 covering ~80% of the entire DRG. A single focal plane was selected to maximize the number of
509 clearly resolvable neurons across the DRG exhibiting robust calcium responses to indentation of
510 the medial hindpaw (saphenous nerve territory). A 30-minute imaging session without external
511 stimulation was conducted to assess spontaneous activity. The neuroma was then surgically
512 exposed following a procedure similar to sciatic nerve exposure during SNT injury. Mechanical
513 stimuli of varying forces were applied to the neuroma using von Frey filaments. Each force was
514 delivered in five trials, with an interstimulus interval of >5 seconds. After imaging the ipsilateral
515 L4 DRG, the same procedure was repeated for the contralateral L4 DRG, except that mechanical
516 stimuli were applied to the intact sciatic nerve at a location corresponding to the neuroma site on
517 the ipsilateral side. The imaging order (i.e., ipsilateral or contralateral first) was randomized to
518 minimize potential variability due to anaesthesia duration. Images were acquired at 10 Hz with a
519 99 ms exposure time during neuroma stimulation. The stimulation was also recorded
520 simultaneously at 25–30 Hz using a digital camera, with the video output time-stamped to
521 synchronize with GCaMP imaging data. For imaging spontaneous activity, exposure time was
522 reduced to 35 ms to minimize photobleaching during long-term recordings. Isoflurane
523 concentration was reduced to 1% throughout the imaging process.

524 Imaging data were analysed using the open-source CaImAn package[57]. Briefly, data were first
525 corrected for motion using the NoRMCorre algorithm. Regions of interest (ROIs) were identified
526 using a constrained non-negative matrix factorization (CNMF) framework, which jointly estimates
527 spatial footprints and temporal activity traces. Extracted fluorescence traces were detrended to
528 correct for bleaching and converted to ΔF/F on a per-cell basis, with baseline (F) defined as the
529 average of the lowest 10% of fluorescence values. Automatically extracted ROIs were reviewed
530 by an investigator to correct false positives and false negatives. The corresponding calcium traces
531 were then evaluated against quality criteria, including spatial correlation, temporal signal-to-noise
532 ratio (ΔF/F exceeding 3× the standard deviation of baseline fluctuation for ≥0.5 s), appropriate rise
533 and decay kinetics, and consistent morphology. Only ROIs meeting these criteria were retained for
534 analysis.

535 To classify spontaneously active cells, neuroma poke–responsive cells, and dual-active cells
536 based on calcium activity, we used an unsupervised clustering approach with Gaussian Mixture
537 Models (GMMs) implemented in Python's scikit-learn package. The model estimated the
538 probability of each cell belonging to one of three classes (Fig. 2g) or two classes (Fig. 3d)
539 according to its peak ΔF/F across the corresponding imaging sessions, with final cluster
540 assignment determined by maximum posterior probability (decision boundary).

541

542 **Miniaturized LED cuff and epineural optogenetic activation**

543 We adapted a previously developed wireless LED array[32] into a wired device to enable behavioural
544 screening across multiple Cre lines (Fig. 4b and Extended Data Fig. 7). The fabrication process for
545 the LED cuff began with the spin-coating of a 3 μm-thick polyimide (PI) layer (HD Microsystems
546 GmbH, catalog no. PI2611) onto a silicon (Si) wafer coated with an aluminum (Al) layer. The

underlying Al acted as a sacrificial layer for subsequent device release. The PI was then baked at 300 °C for 2 hours to complete the imidization process. A 130 nm-thick silicon carbide (SiC) layer was then deposited via plasma-enhanced chemical vapor deposition (PECVD) using an Oxford PlasmaLab System 100 under the following conditions: 133 sccm Ar, 60 sccm CH_4, and 375 sccm of 2% SiH_4 in Ar; RF power of 25 W; substrate temperature of 300 °C; and deposition time of 10 minutes. Next, a metal stack composed of Titanium/Platinum/Gold/Platinum/Titanium (Ti/Pt/Au/Pt/Ti, thicknesses: 10/10/200/10/10 nm) was sputtered using an AC450 system (Alliance-Concept) and patterned by lift-off in an ultrasonic acetone bath (80 kHz, 100% power, 10 minutes). A second 130 nm SiC layer was deposited, followed by spin-coating and baking of an additional PI layer using the same parameters as before. A Titanium/Silicon Oxides (Ti/SiO_2) bilayer (10/25 nm) was subsequently sputtered onto the top PI surface. The final device patterning was carried out using an ICP-RIE etch system (Corial 210IL), defining the shape of the cuff and opening windows for LED integration and soldering. Following the microfabrication steps, solder paste bumps (~50 μm diameter, Chipquik, catalog no. SMDLTLFP10T5) were manually deposited onto the exposed contact pads. Micro-LEDs (Cree Inc., catalog no. DA2432) were placed using a pick-and-place system (JFP Microtechnic) and bonded by heating the wafer on a hotplate at 165 °C, ensuring both electrical and mechanical connections. To improve hermetic sealing, a 15 wt% solution of poly(isobutylene) (PIB, Oppanol, BASF) in cyclohexane (Sigma-Aldrich) was applied to the die surface via pneumatic dispensing. Finally, a 60 μm-thick encapsulating layer of polydimethylsiloxane (PDMS) was printed, baked at 70 °C for 12 hours, and patterned by blade cutting. DC voltage was measured using a source meter (Keithley 2400) while sweeping the input current from 0.5 to 17 mA. Simultaneously, the total optical power output at 470 nm was measured using a calibrated photodiode (S170C, Thorlabs) connected to a power meter console (PM100D,

570 Thorlabs). During measurements, the distance between the photodiode and the micro-LEDs was
571 maintained at approximately 1 mm.

572 The neuroma or intact sciatic nerve was exposed as described in the sciatic nerve injury
573 procedure. The LED cuff was positioned beneath the neuroma or intact sciatic nerve at a
574 perpendicular angle, and its distal end was folded 180° to wrap around the target site. This
575 configuration placed one set of LEDs on the front and the other on the back of the neuroma or
576 nerve (Fig. 4b, right). To secure the device, the two proximal anchoring points were sutured to
577 each other and to the adjacent proximal muscles, while the distal anchoring points were sutured to
578 the upper thigh muscle for additional stabilization (Fig. 4b, right). 10-0 sutures (Ethicon, #2794G)
579 were used for these anchoring sites. The wires with a female nano-miniature circular connector
580 (Omnetics, #A79103-001) were routed subcutaneously to the backside, where a small skin pocket
581 was created to externalize the connector. The thigh incision was closed using 6-0 sutures, while
582 the skin pocket was sealed with tissue adhesive (3M Vetbond, #1469). After each experiment, the
583 placement of the LEDs was confirmed. If displacement occurred (e.g., slippage from the neuroma),
584 the animal was excluded from analysis.

585 The following transgenic lines were used to target sensory neuron subtypes: *Sstr2*$^{T2a-}$
586 ^{CreER}*;Calca-FlpE;R26*$^{LSL-FSF-ReaChR::mCitrine}$ for the Neuroma C-Nociceptor (SSTR2) subtype,
587 *Mrgprd*^{CreER}*;R26*$^{LSL-ReaChR::mCitrine}$ for the C-HTMR/HEAT (MRGPRD) subtype, *Th*$^{T2a-}$
588 ^{CreER}*;Avil*^{FlpO}*;R26*$^{LSL-FSF-ReaChR::mCitrine}$ for the C-LTMR subtype, *Smr2*$^{T2a-Cre}$*;Calca-FlpE;R26*$^{LSL-}$
589 $^{FSF-ReaChR::mCitrine}$ for the Aδ-HTMR/Heat (SMR2) subtype, *TrkB*^{CreER}*;Avil*^{FlpO}*; R26*$^{LSL-FSF-}$
590 $^{ReaChR::mCitrine}$ for the Aδ-LTMR subtype, *Mrgpra3*^{Cre}*;R26*$^{LSL-ReaChR::mCitrine}$ for the C-HTMR/Heat
591 (MRGPRA3) subtype, *Mrgprb4*^{Cre}*;R26*$^{LSL-ReaChR::mCitrine}$ for the C-HTMR/Heat (MRGPRB4)
592 subtype, *Cysltr2*^{Cre}*;R26*$^{LSL-ReaChR::mCitrine}$ for the C-HTMR/Heat (CYSLTR2/SST) subtype,

593 *Trpm8*$^{T2a\text{-}FlpO}$; *R26*$^{FSF\text{-}ReaChR::mCitrine}$ for the C-Cold (TRPM8) subtype. All the mouse lines used to
594 generate these genetic crosses have been previously described: *Sstr2*$^{T2a\text{-}CreER}$ (JAX #039563)[28],
595 *Mrgprd*^{CreER} (JAX #031286)[58], *Th*$^{T2a\text{-}CreER}$ (JAX #025614)[59], *Smr2*$^{T2a\text{-}Cre}$ (JAX #039562)[28],
596 *TrkB*^{CreER} (JAX #027214)[60], *Mrgpra3*^{Cre61}, *Mrgprb4*^{Cre62}, *Cysltr2*^{Cre} (JAX #039985)[28], *Trpm8*$^{T2a\text{-}FlpO}$
597 (JAX #039564[28], *Calca-FlpE*^{63}, *Avil*^{FlpO63}, *R26*$^{LSL\text{-}FSF\text{-}ReaChR::mCitrine}$ (JAX #024846), *R26*$^{LSL\text{-}}$
598 $^{ReaChR::mCitrine}$ (JAX #026294), *R26*$^{FSF\text{-}ReaChR::mCitrine}$ (derived from JAX #024846 by germline
599 excision of LSL cassette). All transgenic mouse lines were maintained on a mixed background and
600 included males and females. CreER lines were induced by a single intraperitoneal injection of
601 tamoxifen dissolved in sunflower seed oil, prepared as previously described[28]. For *Sstr2*$^{T2a\text{-}CreER}$;
602 *Calca-FlpE; R26*$^{LSL\text{-}FSF\text{-}ReaChR::mCitrine}$, we administered 3 mg of tamoxifen at 3–4 weeks;
603 *Mrgprd*^{CreER};*R26*$^{LSL\text{-}ReaChR::mCitrine}$, 2 mg at 3-4 weeks; *Th*$^{T2a\text{-}CreER}$;*Avil*^{FlpO};*R26*$^{LSL\text{-}FSF\text{-}ReaChR::mCitrine}$,
604 2 mg at 3-6 weeks; *TrkB*^{CreER}; *Avil*^{FlpO}; *R26*$^{LSL\text{-}FSF\text{-}ReaChR::mCitrine}$, 0.5 mg at postnatal day 3 to day 5.
605 For optogenetic activation, the external connector was coupled to an adapter linked to a
606 stimulator (AM-Systems, Grass Instruments S88). When mice were in a calm, awake state, a single
607 10 ms pulse was delivered at various voltages corresponding to different optical power levels with
608 behaviours recorded by a high-speed camera at 120 Hz. Each power level was tested in 10 trials
609 with an inter-stimulus interval of >1 minute. Behaviours occurring during stimulation or within 2
610 s after stimulus offset were counted as positive responses. Response probability was calculated as
611 the proportion of trials with a behavioural response out of 10 trials for each animal (Fig. 4c). The
612 occurrence rate of each behaviour type was calculated as the number of trials in which that
613 behaviour was induced from the ipsilateral neuroma site at 60 mW across all animals, divided by
614 the total number of trials (i.e., 10 × number of animals) (Fig. 4d). Response latency (Fig. 4e, left)
615 was defined as the time between opto-stimulation onset (single 10 ms pulse at 60 mW) and the

616 initiation of the behaviour. Single 10 ms pulses were used for all optogenetic experiments except
617 in Extended Data Fig. 9a, where repetitive 10 ms pulses at 10 Hz or continuous light (60 mW)
618 were delivered for 5 s. Cre expression in all animals was verified *post hoc* by histological analysis
619 following completion of optogenetic experiments (Extended Data Fig. 8).

620 Survival analysis using a Cox proportional hazards regression model was used to assess whether
621 flick probability to transcutaneous neuroma pokes predicted the optical threshold for evoked limb
622 flicks. During optogenetic stimulation, optical power (mW) was increased monotonically and
623 treated as the ordered analysis variable, with the first limb flick defined as the event. Animals that
624 did not flick at the maximum tested power (60 mW) were right-censored. Von Frey flick
625 probability (0–1) was included as a continuous covariate. Hazard ratios with 95% confidence
626 intervals were reported, and significance was assessed using the likelihood-ratio test (Fig. 4e, right).
627

628 **Histology**

629 Neuromas, contralateral intact sciatic nerves, or DRG were fixed in 4% paraformaldehyde (PFA)
630 in PBS at 4 °C overnight. Nerves were cryoprotected in 30% sucrose in PBS at 4 °C for one to two
631 days, embedded in OCT compound (Sakura Finetek) on dry ice, and cryosectioned longitudinally
632 (parallel to the axon trajectory) at 50 µm. DRG were fixed and processed for whole-mount staining.
633 Sections or whole DRG were permeabilized in 1% Triton X-100 in PBS for 20 minutes and blocked
634 in 10% normal donkey with 0.3% Triton X-100 in PBS overnight at 4 °C. Primary antibody
635 incubation was performed overnight at 4 °C in blocking solution (1:500) using anti-GFP (Thermo
636 Fisher, #A10262) and anti-PGP9.5 (Abcam, #ab108986). Secondary antibodies were incubated for
637 2 hours at room temperature or overnight at 4 °C in blocking solution (1:500): Cy5-conjugated
638 donkey anti-rabbit (Jackson ImmunoResearch, #711-175-152) and Alexa Fluor 488–conjugated

639 donkey anti-chicken (Jackson ImmunoResearch, #703-545-155). Images were acquired on a Leica
640 SP8 confocal microscope at 1024 × 1024 resolution. Whole DRG were imaged in 60 mm glass-
641 bottom dishes using 10× or 20× air objectives with 2–5 µm z-steps. Neuromas and contralateral
642 nerves were captured by tile scan using a 10× air objective with 2 µm z-steps. Post-processing was
643 performed with LAS X Life Science software (Leica).

644 fibre density (Extended Data Fig. 8) was quantified from mCitrine reporter signal in neuromas
645 and contralateral sciatic nerves using ImageJ. Each neuroma and contralateral nerve typically
646 yielded ~20 and ~12 longitudinal cryosections, respectively; the middle three consecutive slices
647 were selected to minimize epineural tissue interference. Images were converted to 8-bit grayscale,
648 background-subtracted, and thresholded to generate binary masks of axonal fibres. A 50 × 50 µm
649 region of interest (ROI) was placed at the neuroma tip or corresponding contralateral nerve center,
650 and the axon-occupied area within this ROI was measured. fibre density was expressed as the
651 fraction of axon-positive area relative to total ROI area. Values from three slices were averaged to
652 obtain one measurement per sample.

653

654 ***In situ* hybridization combined with immunohistochemistry**

655 L4 DRG were dissected under 2% isoflurane anaesthesia and embedded in OCT on dry ice. The
656 tissues were then cryosectioned at a thickness of 20 µm and stored at -80°C until processing. To
657 assess the co-expression of *Sstr2* mRNA and mCitrine protein (Extended Data Fig. 9b), *in situ*
658 hybridization (ISH) was performed using the RNAscope (Advanced Cell Diagnostics) combined
659 with immunohistochemistry (IHC). Sections were processed according to the manufacturer's ISH
660 instructions using the RNAscope H2O2 and Protease Reagents, the RNAscope Multiplex
661 Fluorescent Detection Kit v2, with *Sstr2* (Cat. # 437681-C2) detected via Akoya Opal Dye 570.

662 Immediately following the RNAscope protocol, IHC was performed to detect mCitrine expression.
663 Briefly, slides were blocked with 10% Normal Donkey Serum with PBST (1X PBS with 0.1%
664 Tween20) for 15 minutes at room temperature. Primary antibody incubation was performed for 1
665 hr at room temperature in blocking solution using goat anti-GFP antibody (1:500; US Biological
666 Life Sciences, G8965-01E). Following two 5-minute rinses in PBST, secondary antibodies
667 incubation was performed for 40 min at room temperature in blocking solution using Donkey anti-
668 Goat Alexa Fluor 488 (ThermoFisher Scientific, A-11055). After the final washes, sections were
669 counterstained with DAPI and coverslipped. Confocal images were acquired using a Zeiss LSM
670 900 microscope equipped with 10X and 20X air objectives.

671

672 **snRNA-seq of DRG across pain conditions**

673 From a parent cohort of 60 mice, L4 and L5 DRG were collected from 18 mice (9 males and 9
674 females) that consistently exhibited a high-pain phenotype across 8–10 weeks post-SNT, with
675 phenotyping performed weekly and tissue collected at 10 weeks, and from 18 mice (9 males and
676 9 females) that consistently exhibited a low-pain phenotype over the same period. 36 contralateral
677 L4 and L5 DRG from both high- and low-pain mice were combined as the control group.

678 All nuclear extraction steps were performed on ice, or at 4 °C. Frozen L4 and L5 DRG, collected
679 on dry ice in DNA/RNA LoBind tubes (Qiagen) were homogenized in NST buffer: 50 ml NST
680 buffer contained 25 ml of 2x ST buffer, 1ml of 10% IGPAL, 1.4 ml of 35% BSA, and 22.6 ml
681 nuclease-free water, and was prepared from ST buffer, containing 146 mM NaCl, 10 mM Tris-HCl,
682 pH 7.5, 1 mM $CaCl_2$, and 21 mM $MgCl_2$[64]. For each sample, 7.5 ml of ST and 7.5 ml of NST
683 buffer were prepared and 10 µl of Rnasin was added to each. For each sample, 1 ml cold NST
684 buffer (on ice) was added directly to the tube containing frozen DRG, allowed to thaw for 15–30

seconds, and DRG were transferred to a 7 ml Dounce Wheaton homogenizer containing 4 ml of NST buffer, and homogenized with 5 strokes with the loose pestle and 15 strokes with the tight pestle. The homogenate was then filtered through a 40 µm cell filter into a 50 ml Falcon tube on ice. 5 ml of ST buffer was added to the homogenizer, and any remaining homogenate was collected and also pipetted through the 40 µm cell filter. 10 ml of filtered homogenate then filtered through a 20 µm cell filter into a 15 ml Falcon tube on ice. The homogenizer was thoroughly rinsed between samples. Samples were centrifuged at 500 × g for 10 minutes at 4 °C. The supernatant was removed and the pellet was resuspended in 1 ml of ST buffer. 10 µl of Hoechst was added for a final concentration of 0.5 µg/ml, and the samples were FACS sorted to isolate nuclei.

Nuclei suspensions were sequenced using 10x Genomics assays, resuspended, and loaded into the 10x Chromium device for snRNA-seq (10x Genomics 3' v3). Libraries were prepared for snRNA-seq according to the manufacturer's protocol. Libraries were sequenced on an Illumina NovaSeqX (Azenta). Sequencing data were processed and mapped to the mouse (mm10) genome using 10x Genomics cellranger v9 using default parameters. We ran the remove-background function of Cellbender (v0.3.0) to remove ambient RNA and empty droplets from raw expression matrices using default parameters.

We followed a similar cell type annotation and clustering approach as previously described[30,47], and adopted the established physiological nomenclature for each neuronal subtype as shown in Table 1 in a reference study[28]. Seurat v4 was used to perform quality control, data normalization, cell type annotation and comparison between neuroma conditions[65]. Nuclei with >1000 genes and <10% of mitochondrial counts were included for analysis. We found 2000 variable genes for each library after log-normalization, and then integration anchors were selected across all libraries. The data were then scaled, and we selected PCs on the basis of the point where the PC only contributes

708 to 5% of SD of highly variable gene expression and all PCs cumulatively contributed to 90% of
709 the SD of highly variable gene expression. The libraries were then integrated using Seurat's CCA
710 algorithm, and nuclei were clustered and plotted in UMAP space at a resolution of 0.5. A Wilcoxon
711 rank sum test was performed between the clusters to identify marker genes. We annotated clusters
712 that were *Snap25*$^{+}$ ($\log_2$FC > 0.5 and adjusted *P* value < 0.05 relative to all other clusters) as
713 "neurons" and clusters that were *Sparc*$^{+}$ ($\log_2$FC > 0.5 and adjusted *P* value < 0.05 relative to all
714 other clusters) as "non-neurons." Neurons were then separated and reintegrated using a resolution
715 of 1. We annotated neurons using marker gene expression (Extended Data Fig. 6a; $\log_2$FC > 0.5;
716 adjusted p-value < 0.05 relative to all other clusters). Clusters were labelled as doublets if they
717 contained both expression of *Snap25*, *Mpz*, and *Sparc* ($\log_2$FC > 0.5 and adjusted *P* value < 0.05
718 relative to all other clusters). Doublets were then removed, and the nuclei were reintegrated using
719 the same parameters as described and then reannotated for a final time. To identify genes
720 differentially expressed between conditions within each subtype, we used the Wilcoxon rank-sum
721 test.

722 Directional concordance scores for each gene within each cell type were computed from its $\log_2$
723 fold-change ($\log_2$FC) values between the high-pain vs. low-pain and high-pain vs. control
724 comparisons (Extended Data Fig. 6c), defined as:

725
$$\begin{cases} +\sqrt{|\log_2\mathrm{FC}_{\text{high pain/low pain}} \cdot \log_2\mathrm{FC}_{\text{high pain/control}}|}, \text{if both } \log_2\mathrm{FC} > 0 \text{ (upregulated in both)} \\ -\sqrt{|\log_2\mathrm{FC}_{\text{high pain/low pain}} \cdot \log_2\mathrm{FC}_{\text{high pain/control}}|}, \text{if both } \log_2\mathrm{FC} < 0 \text{ (downregulated in both)} \\ 0, \text{otherwise (opposite directions or no change)} \end{cases}$$

726 For gene ontology (GO) analysis, we used EnrichR [66] to assess functional enrichment. We
727 selected genes significantly enriched in the Neuroma C-Nociceptor (SSTR2) population under the
728 high pain condition ($\log_2$FC > 0.5; adjusted p < 0.05), compared to either the Neuroma C-

729 Nociceptor (SSTR2) cells in the low-pain condition or the contralateral control condition. As the
730 background gene list, we used all genes expressed in the Neuroma C-Nociceptor (SSTR2)
731 population.
732
733 **Statistical analysis**
734 All statistical analyses, except for snRNA-seq data, were performed using GraphPad Prism, with
735 the exact tests and *P* values reported in the figures, figure legends, or source data.
736
737 **Data availability**
738 All data supporting the findings of this study are available within the manuscript. Reagents are
739 available from the corresponding authors upon reasonable request. snRNA-seq will be deposited
740 into GEO upon manuscript acceptance.

741 **Acknowledgements** We thank Dr. Bruce P. Bean and members of the Ginty and Woolf laboratories
742 for their constructive feedback. We thank Kitwa Ng for helpful comments on the manuscript. We
743 also thank the IDDRC Animal Behavior and Physiology Core, funded by NIH/NICHD
744 P50HD105351 and IDDRC Cellular Imaging Core, funded by NIH P50 HD105351 at Boston
745 Children's Hospital. Schematics and illustrations were created with BioRender.com. This work
746 was supported by the International Human Frontier Science Program Organization LT0026/2023-
747 L (X.Z.), NIH grants R35NS105076 (C.J.W.), R35NS097344 (D.D.G.), R35NS132196 (D.D.G.),
748 and R01AT011447 (D.D.G. and C.J.W.), the Edward R. and Anne G. Lefler Center for
749 Neurodegenerative Disorders (D.D.G.), and the K. Lisa Yang Brain Body Center at Harvard
750 Medical School (D.D.G.). D.D.G. is an investigator of the Howard Hughes Medical Institute. This
751 article is subject to HHMI's Open Access to Publications policy. HHMI lab heads have previously
752 granted a nonexclusive CC BY 4.0 license to the public and a sublicensable license to HHMI in
753 their research articles. Pursuant to those licenses, the author-accepted manuscript of this article can
754 be made freely available under a CC BY 4.0 license immediately upon publication.
755
756 **Author contributions** X.Z., D.D.G., and C.J.W. conceived the study. X.Z. performed all
757 experiments and analysed the data, with assistance from R.M.G. (generation of transgenic mouse
758 lines and *in situ* hybridization), S.A.B. (snRNA-seq), K.H. (histology), N.M.B., E.B., E.S.
759 (behavioural studies and histology), K.W. (LED cuff design), O.B. (automated behavioural screen),
760 B.L.T. (acute pain experiments), S.S.J., B.G.E. (tissue collection for snRNA-seq), M.Q.H. (home-
761 cage EMG setup), C.S. (Piezo2-knockout experiments), K.L. (generation of transgenic mouse lines
762 and *in situ* hybridization), E.O.A. (generation of transgenic mouse lines), and I.F. (LED cuff
763 calibration). A.R. provided resource for the home-cage EMG experiments. B.R.J. provided

764 expertise on and assisted with the transcutaneous neuroma poke tests. B.J.W. provided expertise
765 on the behavioural experiments. W.R. provided resource and oversight of the snRNA-seq
766 experiments. S.P.L. provided resource and oversight of LED cuff design. D.D.G. and C.J.W.
767 supervised the project. X.Z., D.D.G., and C.J.W. wrote the manuscript with input from all authors.
768

769 **Competing interests** X.Z., D.D.G., and C.J.W. are consultants for Alive Molecular Technologies,
770 Inc. D.D.G. is a founder of Krause Therapeutics, and C.J.W. is a founder of Nocion Therapeutics,
771 Quralis, and BlackBox Bio, and serves on the scientific advisory boards of Lundbeck Pharma,
772 Axonis, Niroda, Mimetic Medicine, Tenvie Therapeutics, and Tafalgie Therapeutics.

773 # References

774 1 Bouhassira, D. *et al*. Comparison of pain syndromes associated with nervous or
775 somatic lesions and development of a new neuropathic pain diagnostic
776 questionnaire (DN4). *Pain* **114**, 29-36 (2005).
777 https://doi.org/10.1016/j.pain.2004.12.010
778 2 Bouhassira, D. *et al*. Development and validation of the Neuropathic Pain Symptom
779 Inventory. *Pain* **108**, 248-257 (2004). https://doi.org/10.1016/j.pain.2003.12.024
780 3 Maier, C. *et al*. Quantitative sensory testing in the German Research Network on
781 Neuropathic Pain (DFNS): somatosensory abnormalities in 1236 patients with
782 different neuropathic pain syndromes. *Pain* **150**, 439-450 (2010).
783 https://doi.org/10.1016/j.pain.2010.05.002
784 4 Buch, N. S., Qerama, E., Brix Finnerup, N. & Nikolajsen, L. Neuromas and
785 postamputation pain. *Pain* **161**, 147-155 (2020).
786 https://doi.org/10.1097/j.pain.0000000000001705
787 5 Hwang, C. D. *et al*. Biology and pathophysiology of symptomatic neuromas. *Pain* **165**,
788 550-564 (2024). https://doi.org/10.1097/j.pain.0000000000003055
789 6 Sandkuhler, J. Models and mechanisms of hyperalgesia and allodynia. *Physiol Rev* **89**,
790 707-758 (2009). https://doi.org/10.1152/physrev.00025.2008
791 7 Tappe-Theodor, A. & Kuner, R. Studying ongoing and spontaneous pain in rodents--
792 challenges and opportunities. *Eur J Neurosci* **39**, 1881-1890 (2014).
793 https://doi.org/10.1111/ejn.12643
794 8 Langford, D. J. *et al*. Coding of facial expressions of pain in the laboratory mouse. *Nat*
795 *Methods* **7**, 447-449 (2010). https://doi.org/10.1038/nmeth.1455
796 9 King, T. *et al*. Unmasking the tonic-aversive state in neuropathic pain. *Nat Neurosci*
797 **12**, 1364-1366 (2009). https://doi.org/10.1038/nn.2407
798 10 Attal, N. *et al*. Neuropathic pain: are there distinct subtypes depending on the
799 aetiology or anatomical lesion? *Pain* **138**, 343-353 (2008).
800 https://doi.org/10.1016/j.pain.2008.01.006
801 11 Zheng, Q. *et al*. Synchronized cluster firing, a distinct form of sensory neuron
802 activation, drives spontaneous pain. *Neuron* **110**, 209-220 e206 (2022).
803 https://doi.org/10.1016/j.neuron.2021.10.019
804 12 Djouhri, L., Koutsikou, S., Fang, X., McMullan, S. & Lawson, S. N. Spontaneous pain,
805 both neuropathic and inflammatory, is related to frequency of spontaneous firing in
806 intact C-fiber nociceptors. *J Neurosci* **26**, 1281-1292 (2006).
807 https://doi.org/10.1523/JNEUROSCI.3388-05.2006
808 13 Gangadharan, V. *et al*. Neuropathic pain caused by miswiring and abnormal end
809 organ targeting. *Nature* **606**, 137-145 (2022). https://doi.org/10.1038/s41586-022-
810 04777-z
811 14 Wu, G. *et al*. Early onset of spontaneous activity in uninjured C-fiber nociceptors after
812 injury to neighboring nerve fibers. *J Neurosci* **21**, RC140 (2001).
813 https://doi.org/10.1523/JNEUROSCI.21-08-j0002.2001

15 Wu, G. *et al*. Degeneration of myelinated efferent fibers induces spontaneous activity in uninjured C-fiber afferents. *J Neurosci* **22**, 7746-7753 (2002). https://doi.org/10.1523/JNEUROSCI.22-17-07746.2002

16 Kehlet, H., Jensen, T. S. & Woolf, C. J. Persistent postsurgical pain: risk factors and prevention. *Lancet* **367**, 1618-1625 (2006). https://doi.org/10.1016/S0140-6736(06)68700-X

17 Fillingim, R. B. Individual differences in pain: understanding the mosaic that makes pain personal. *Pain* **158 Suppl 1**, S11-S18 (2017). https://doi.org/10.1097/j.pain.0000000000000775

18 Barkai, O. *et al*. A machine learning tool with light-based image analysis for automatic classification of 3D pain behaviours. *Cell Rep Methods*, 101145 (2025). https://doi.org/10.1016/j.crmeth.2025.101145

19 Su, P. P., He, L., Zhang, L., Yu, J. & Guan, Z. Saphenous-sural nerve injury: a sensory-specific rodent model of neuropathic pain without motor deficits. *Pain* (2025). https://doi.org/10.1097/j.pain.0000000000003722

20 Bumgarner, J. R., Walker, W. H., 2nd & Nelson, R. J. Circadian rhythms and pain. *Neurosci Biobehav Rev* **129**, 296-306 (2021). https://doi.org/10.1016/j.neubiorev.2021.08.004

21 Oliveira, K. M. C. *et al*. Time course of traumatic neuroma development. *PLoS One* **13**, e0200548 (2018). https://doi.org/10.1371/journal.pone.0200548

22 Arnold, D. M. J. *et al*. Diagnostic Criteria for Symptomatic Neuroma. *Ann Plast Surg* **82**, 420-427 (2019). https://doi.org/10.1097/SAP.0000000000001796

23 Miclescu, A., Schmelz, M. & Gordh, T. Differential analgesic effects of subanesthetic concentrations of lidocaine on spontaneous and evoked pain in human painful neuroma: A randomized, double blind study. *Scand J Pain* **8**, 37-44 (2015). https://doi.org/10.1016/j.sjpain.2015.04.026

24 Roza, C., Laird, J. M., Souslova, V., Wood, J. N. & Cervero, F. The tetrodotoxin-resistant Na+ channel Nav1.8 is essential for the expression of spontaneous activity in damaged sensory axons of mice. *J Physiol* **550**, 921-926 (2003). https://doi.org/10.1113/jphysiol.2003.046110

25 Choi, D. *et al*. Spontaneous activity in peripheral sensory nerves: a systematic review. *Pain* **165**, 983-996 (2024). https://doi.org/10.1097/j.pain.0000000000003115

26 Decosterd, I. & Woolf, C. J. Spared nerve injury: an animal model of persistent peripheral neuropathic pain. *Pain* **87**, 149-158 (2000). https://doi.org/10.1016/S0304-3959(00)00276-1

27 Usoskin, D. *et al*. Unbiased classification of sensory neuron types by large-scale single-cell RNA sequencing. *Nat Neurosci* **18**, 145-153 (2015). https://doi.org/10.1038/nn.3881

28 Qi, L. *et al*. A mouse DRG genetic toolkit reveals morphological and physiological diversity of somatosensory neuron subtypes. *Cell* **187**, 1508-1526 e1516 (2024). https://doi.org/10.1016/j.cell.2024.02.006

29 Sharma, N. *et al*. The emergence of transcriptional identity in somatosensory neurons. *Nature* **577**, 392-398 (2020). https://doi.org/10.1038/s41586-019-1900-1

30 Bhuiyan, S. A. *et al*. Harmonized cross-species cell atlases of trigeminal and dorsal root ganglia. *Sci Adv* **10**, eadj9173 (2024). https://doi.org/10.1126/sciadv.adj9173

31 Krauter, D. *et al*. Spatial organization, chromatin accessibility and gene-regulatory programs defining mouse sensory neurons. *Commun Biol* **8**, 908 (2025). https://doi.org/10.1038/s42003-025-08315-1

32 Michoud, F. *et al*. Epineural optogenetic activation of nociceptors initiates and amplifies inflammation. *Nat Biotechnol* **39**, 179-185 (2021). https://doi.org/10.1038/s41587-020-0673-2

33 Wolfson, R. L. *et al*. DRG afferents that mediate physiologic and pathologic mechanosensation from the distal colon. *Cell* **186**, 3368-3385 e3318 (2023). https://doi.org/10.1016/j.cell.2023.07.007

34 Bhuiyan, S. A. *et al*. A Reference Atlas of the Human Dorsal Root Ganglion. *bioRxiv* (2025). https://doi.org/10.1101/2025.11.05.686654

35 Lezgiyeva, K. *et al*. Fast-conducting mechanonociceptors uniquely engage reflexive and affective pain circuitry to drive protective responses. *bioRxiv* (2025). https://doi.org/10.1101/2025.11.11.687663

36 Cooper, A. H. *et al*. Peripheral nerve injury results in a biased loss of sensory neuron subpopulations. *Pain* **165**, 2863-2876 (2024). https://doi.org/10.1097/j.pain.0000000000003321

37 Dhandapani, R. *et al*. Control of mechanical pain hypersensitivity in mice through ligand-targeted photoablation of TrkB-positive sensory neurons. *Nat Commun* **9**, 1640 (2018). https://doi.org/10.1038/s41467-018-04049-3

38 Yarmolinsky, D. A. *et al*. Differential modification of ascending spinal outputs in acute and chronic pain states. *Neuron* **113**, 1223-1239 e1225 (2025). https://doi.org/10.1016/j.neuron.2025.01.031

39 Murthy, S. E. *et al*. The mechanosensitive ion channel Piezo2 mediates sensitivity to mechanical pain in mice. *Sci Transl Med* **10** (2018). https://doi.org/10.1126/scitranslmed.aat9897

40 Gottrup, H., Bach, F. W., Juhl, G. & Jensen, T. S. Differential effect of ketamine and lidocaine on spontaneous and mechanical evoked pain in patients with nerve injury pain. *Anesthesiology* **104**, 527-536 (2006). https://doi.org/10.1097/00000542-200603000-00021

41 Murai, N. *et al*. Spontaneous and evoked pain-associated behaviours in a rat model of neuropathic pain respond differently to drugs with different mechanisms of action. *Pharmacol Biochem Behav* **141**, 10-17 (2016). https://doi.org/10.1016/j.pbb.2015.11.008

42 Deseure, K. & Hans, G. H. Differential drug effects on spontaneous and evoked pain behaviour in a model of trigeminal neuropathic pain. *J Pain Res* **10**, 279-286 (2017). https://doi.org/10.2147/JPR.S124526

43 Hung, C. H., Wang, J. C. & Strichartz, G. R. Spontaneous Chronic Pain After Experimental Thoracotomy Revealed by Conditioned Place Preference: Morphine Differentiates Tactile Evoked Pain From Spontaneous Pain. *J Pain* **16**, 903-912 (2015). https://doi.org/10.1016/j.jpain.2015.06.006

44 Zeng, X., Powell, R. & Woolf, C. J. Mechanism-based nonopioid analgesic targets. *J Clin Invest* **135** (2025). https://doi.org/10.1172/JCI191346

45 Madigan, V., Zhang, F. & Dahlman, J. E. Drug delivery systems for CRISPR-based genome editors. *Nat Rev Drug Discov* **22**, 875-894 (2023). https://doi.org/10.1038/s41573-023-00762-x

46 Raj, A. & van Oudenaarden, A. Nature, nurture, or chance: stochastic gene expression and its consequences. *Cell* **135**, 216-226 (2008). https://doi.org/10.1016/j.cell.2008.09.050

47 Renthal, W. *et al*. Transcriptional Reprogramming of Distinct Peripheral Sensory Neuron Subtypes after Axonal Injury. *Neuron* **108**, 128-144 e129 (2020). https://doi.org/10.1016/j.neuron.2020.07.026

48 Znaor, L., Lovric, S., Hogan, Q. & Sapunar, D. Association of neural inflammation with hyperalgesia following spinal nerve ligation. *Croat Med J* **48**, 35-42 (2007).

49 Yan, H., Gao, W., Pan, Z., Zhang, F. & Fan, C. The expression of alpha-SMA in the painful traumatic neuroma: potential role in the pathobiology of neuropathic pain. *J Neurotrauma* **29**, 2791-2797 (2012). https://doi.org/10.1089/neu.2012.2502

50 Deininger, S. *et al*. Nerve injury converts Schwann cells in a long-term repair-like state in human neuroma tissue. *Exp Neurol* **382**, 114981 (2024). https://doi.org/10.1016/j.expneurol.2024.114981

51 Khan, J., Noboru, N., Young, A. & Thomas, D. Pro and anti-inflammatory cytokine levels (TNF-alpha, IL-1beta, IL-6 and IL-10) in rat model of neuroma. *Pathophysiology* **24**, 155-159 (2017). https://doi.org/10.1016/j.pathophys.2017.04.001

52 Austin, P. J. *et al*. Evidence for a distinct neuro-immune signature in rats that develop behavioural disability after nerve injury. *J Neuroinflammation* **12**, 96 (2015). https://doi.org/10.1186/s12974-015-0318-4

53 Zhang, Z. *et al*. Automated preclinical detection of mechanical pain hypersensitivity and analgesia. *Pain* **163**, 2326-2336 (2022). https://doi.org/10.1097/j.pain.0000000000002680

54 Chaplan, S. R., Bach, F. W., Pogrel, J. W., Chung, J. M. & Yaksh, T. L. Quantitative assessment of tactile allodynia in the rat paw. *J Neurosci Methods* **53**, 55-63 (1994). https://doi.org/10.1016/0165-0270(94)90144-9

55 Santiago, C. *et al*. Activity-dependent development of the body's touch receptors. *Neuron* **113**, 1758-1773 e1759 (2025). https://doi.org/10.1016/j.neuron.2025.04.015

56 Nonomura, K. *et al*. Piezo2 senses airway stretch and mediates lung inflation-induced apnoea. *Nature* **541**, 176-181 (2017). https://doi.org/10.1038/nature20793

57 Giovannucci, A. *et al*. CaImAn an open source tool for scalable calcium imaging data analysis. *Elife* **8** (2019). https://doi.org/10.7554/eLife.38173

58 Olson, W. *et al*. Sparse genetic tracing reveals regionally specific functional organization of mammalian nociceptors. *Elife* **6** (2017). https://doi.org/10.7554/eLife.29507

59 Abraira, V. E. *et al*. The Cellular and Synaptic Architecture of the Mechanosensory Dorsal Horn. *Cell* **168**, 295-310 e219 (2017). https://doi.org/10.1016/j.cell.2016.12.010

60 Rutlin, M. *et al*. The cellular and molecular basis of direction selectivity of Adelta-LTMRs. *Cell* **159**, 1640-1651 (2014). https://doi.org/10.1016/j.cell.2014.11.038

61 Han, L. *et al*. A subpopulation of nociceptors specifically linked to itch. *Nat Neurosci* **16**, 174-182 (2013). https://doi.org/10.1038/nn.3289

62 Vrontou, S., Wong, A. M., Rau, K. K., Koerber, H. R. & Anderson, D. J. Genetic identification of C fibres that detect massage-like stroking of hairy skin in vivo. *Nature* **493**, 669-673 (2013). https://doi.org/10.1038/nature11810

63 Choi, S. *et al*. Parallel ascending spinal pathways for affective touch and pain. *Nature* **587**, 258-263 (2020). https://doi.org/10.1038/s41586-020-2860-1

64 Slyper, M. *et al*. A single-cell and single-nucleus RNA-Seq toolbox for fresh and frozen human tumors. *Nat Med* **26**, 792-802 (2020). https://doi.org/10.1038/s41591-020-0844-1

65 Hao, Y. *et al*. Integrated analysis of multimodal single-cell data. *Cell* **184**, 3573-3587 e3529 (2021). https://doi.org/10.1016/j.cell.2021.04.048

66 Chen, E. Y. *et al*. Enrichr: interactive and collaborative HTML5 gene list enrichment analysis tool. *BMC Bioinformatics* **14**, 128 (2013). https://doi.org/10.1186/1471-2105-14-128

67 Burek, D. J. *et al*. Inflammatory pain in mice induces light cycle-dependent effects on sleep architecture. *Neuropsychopharmacology* **50**, 1595-1605 (2025). https://doi.org/10.1038/s41386-025-02152-w

Fig.1

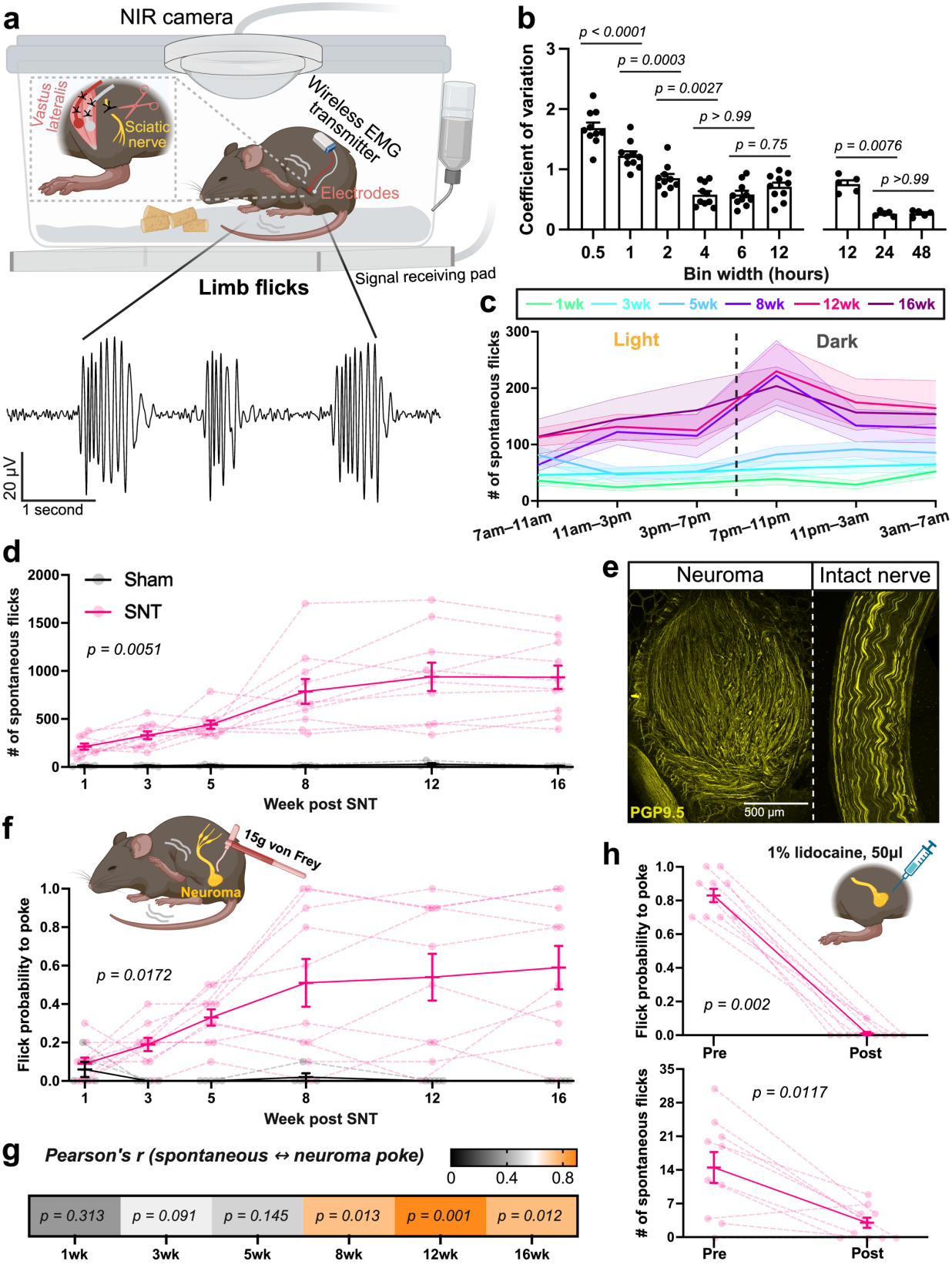
a
NIR camera
Vastus lateralis
Sciatic nerve
Wireless EMG transmitter
Electrodes
Signal receiving pad
Limb flicks
20 µV
1 second
b
Coefficient of variation
p < 0.0001
p = 0.0003
p = 0.0027
p > 0.99
p = 0.75
p = 0.0076
p >0.99
0.5 1 2 4 6 12 12 24 48
Bin width (hours)
c
1wk 3wk 5wk 8wk 12wk 16wk
Light
Dark
# of spontaneous flicks
7am–11am 11am–3pm 3pm–7pm 7pm–11pm 11pm–3am 3am–7am
d
Sham
SNT
p = 0.0051
# of spontaneous flicks
Week post SNT
e
Neuroma
Intact nerve
PGP9.5
500 µm
f
15g von Frey
Neuroma
Flick probability to poke
p = 0.0172
Week post SNT
g
Pearson's r (spontaneous ↔ neuroma poke)
0 0.4 0.8
p = 0.313 p = 0.091 p = 0.145 p = 0.013 p = 0.001 p = 0.012
1wk 3wk 5wk 8wk 12wk 16wk
h
1% lidocaine, 50µl
Flick probability to poke
p = 0.002
Pre Post
# of spontaneous flicks
p = 0.0117
Pre Post

964

Fig. 1 | Neuromas drive chronic spontaneous neuropathic pain. a, Schematic of the home-cage EMG/video recording system (top) and representative EMG trace of limb flick bouts (bottom) after SNT. **b**, Coefficient of variation (CV) of spontaneous limb flick counts following binning of 24-hour recordings into different time windows (0.5, 1, 2, 4, 6, and 12 hours). Each dot represents one recording from an SNT mouse (n = 10). A subset of five mice was recorded for 6 consecutive days to compute CV across extended 12-, 24-, and 48-hour windows. Data are mean ± SEM. *P* values from one-way ANOVA with Tukey's multiple comparisons within each dataset. **c**, Spontaneous limb flick counts quantified in 4-hour bins over 24 hours at indicated time points post-SNT. Light phase: 7:00 a.m.–7:00 p.m.; dark phase: 7:00 p.m.–7:00 a.m. Solid lines and shaded bands represent mean ± SEM across n = 10 SNT mice. **d**, Total 24-hour spontaneous flick counts in individual mice after sham surgery (n = 5) or SNT (n = 10). Data are mean ± SEM; dashed lines connect individual mice. *P* values from two-way ANOVA with Tukey's multiple comparisons (figure shows the interaction effect of sham vs SNT over time). **e**, Confocal images of a neuroma (8 weeks post-SNT) and contralateral intact nerve labelled with a neuronal axonal marker PGP9.5. **f**, Flick probability in response to transcutaneous neuroma poke after sham surgery or SNT in the same mice shown in (**d**). **g**, Pearson's correlation between spontaneous flick counts (**d**) and flick probability (**f**) at indicated time points post-SNT. **h**, Flick probability to poke (top) and spontaneous flick counts over 30 minutes (bottom) before and after local lidocaine injection at the neuroma site (8–12 weeks post-SNT, n = 10 high-pain mice). Data are mean ± SEM; dashed lines connect individual mice. *P* values from two-sided Wilcoxon matched-pairs signed-rank test.

Fig.2

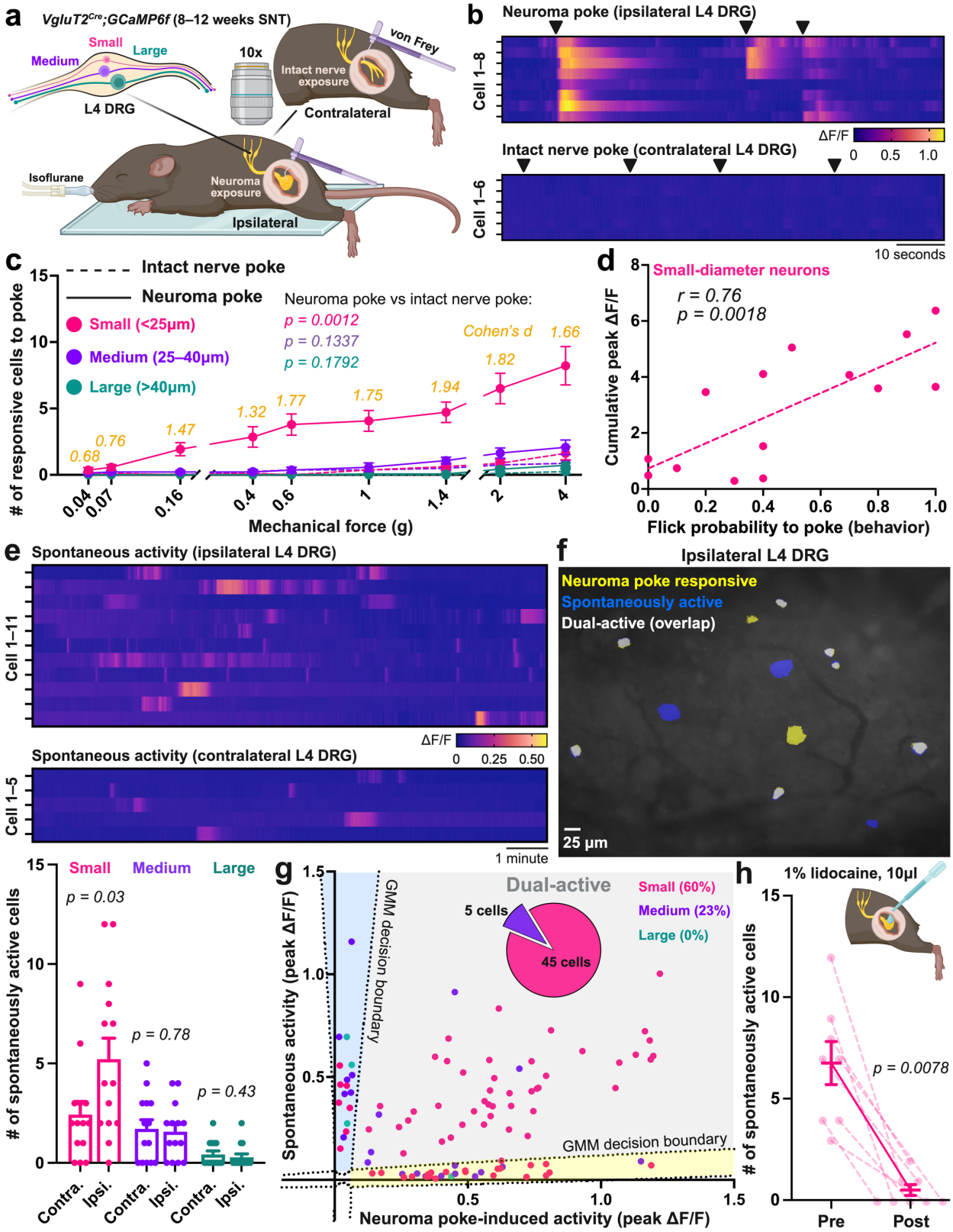
a
VgluT2Cre;GCaMP6f (8–12 weeks SNT)
Small
Large
Medium
L4 DRG
10x
von Frey
Intact nerve exposure
Contralateral
Isoflurane
Neuroma exposure
Ipsilateral
b
Neuroma poke (ipsilateral L4 DRG)
Cell 1–8
ΔF/F
0
0.5
1.0
Intact nerve poke (contralateral L4 DRG)
Cell 1–6
10 seconds
c
Intact nerve poke
Neuroma poke
Small (<25μm)
Medium (25–40μm)
Large (>40μm)
Neuroma poke vs intact nerve poke:
p = 0.0012
p = 0.1337
p = 0.1792
Cohen's d
0.68
0.76
1.47
1.32
1.77
1.75
1.94
1.82
1.66
# of responsive cells to poke
Mechanical force (g)
d
Small-diameter neurons
r = 0.76
p = 0.0018
Cumulative peak ΔF/F
Flick probability to poke (behavior)
e
Spontaneous activity (ipsilateral L4 DRG)
Cell 1–11
ΔF/F
0
0.25
0.50
Spontaneous activity (contralateral L4 DRG)
Cell 1–5
1 minute
f
Ipsilateral L4 DRG
Neuroma poke responsive
Spontaneously active
Dual-active (overlap)
25 μm
Small
Medium
Large
p = 0.03
p = 0.78
p = 0.43
# of spontaneously active cells
Contra.
Ipsi.
g
Dual-active
5 cells
45 cells
Small (60%)
Medium (23%)
Large (0%)
GMM decision boundary
GMM decision boundary
Spontaneous activity (peak ΔF/F)
Neuroma poke-induced activity (peak ΔF/F)
h
1% lidocaine, 10μl
p = 0.0078
# of spontaneously active cells
Pre
Post

984

985 **Fig. 2 | Small-diameter DRG neurons respond to neuroma poke and exhibit ectopic spontaneous**
986 **activity. a**, Schematic of the *in vivo* DRG imaging setup. **b**, Calcium activity heatmaps from individual
987 DRG neurons from one representative mouse in response to a 1.4 g von Frey filament applied to the
988 neuroma or to the contralateral intact nerve. Arrowheads indicate stimulus timing. For intact nerve poke,
989 cells were defined by responses to plantar paw stimulation with the same filament, as no cells showed
990 detectable responses to the nerve poke. **c**, Quantification of responsive cells by soma diameter, small (<25
991 μm), medium (25–40 μm), and large (>40 μm), across a range of mechanical forces applied with von Frey
992 filaments. Data are mean ± SEM from 14 ipsilateral and contralateral L4 DRG (n = 14 mice). *P* values from
993 two-way ANOVA with Tukey's multiple comparisons (figure shows the interaction effect of neuroma poke
994 vs intact nerve poke across mechanical forces). Cohen's d effect sizes are shown for small-diameter neurons
995 (neuroma poke versus intact nerve poke). **d**, Pearson's correlation between the cumulative peak ΔF/F of
996 responsive small-diameter DRG neurons to neuroma poke (1.4 g von Frey) and behavioural flick probability
997 to transcutaneous neuroma poke. Each dot represents one mouse. **e**, Representative heatmaps of
998 spontaneous calcium activity from individual neurons from one representative mouse in ipsilateral and
999 contralateral L4 DRG (top), and quantification of spontaneously active cells of each size during 30-minute
1000 recordings (bottom). Data are mean ± SEM; each dot represents one L4 DRG (n = 14 DRG from 14 mice).
1001 *P* values from two-sided paired t-tests. **f**, Example overlay of cells spontaneously active (blue) and cells
1002 responsive to neuroma poke (yellow); dual-active cells are overlaid (white). **g**, Classification of cells solely
1003 responsive to neuroma poke, solely spontaneously active, or dual-active, based on peak activity amplitude
1004 determined by Gaussian Mixture Model (GMM) boundaries (dashed lines). Percentages indicate the
1005 proportion of dual-active cells relative to the total number of cells of each size. Pie chart depicts the cell
1006 distribution within the dual-active category. Each dot represents one cell. **h**, Number of spontaneously
1007 active small-diameter cells before and 5 minutes after topical application of lidocaine to the neuroma. Data
1008 are mean ± SEM; dashed lines connect ipsilateral L4 DRG from individual mice (n = 8). *P* value from two-
1009 sided Wilcoxon matched-pairs signed-rank test.

Fig.3

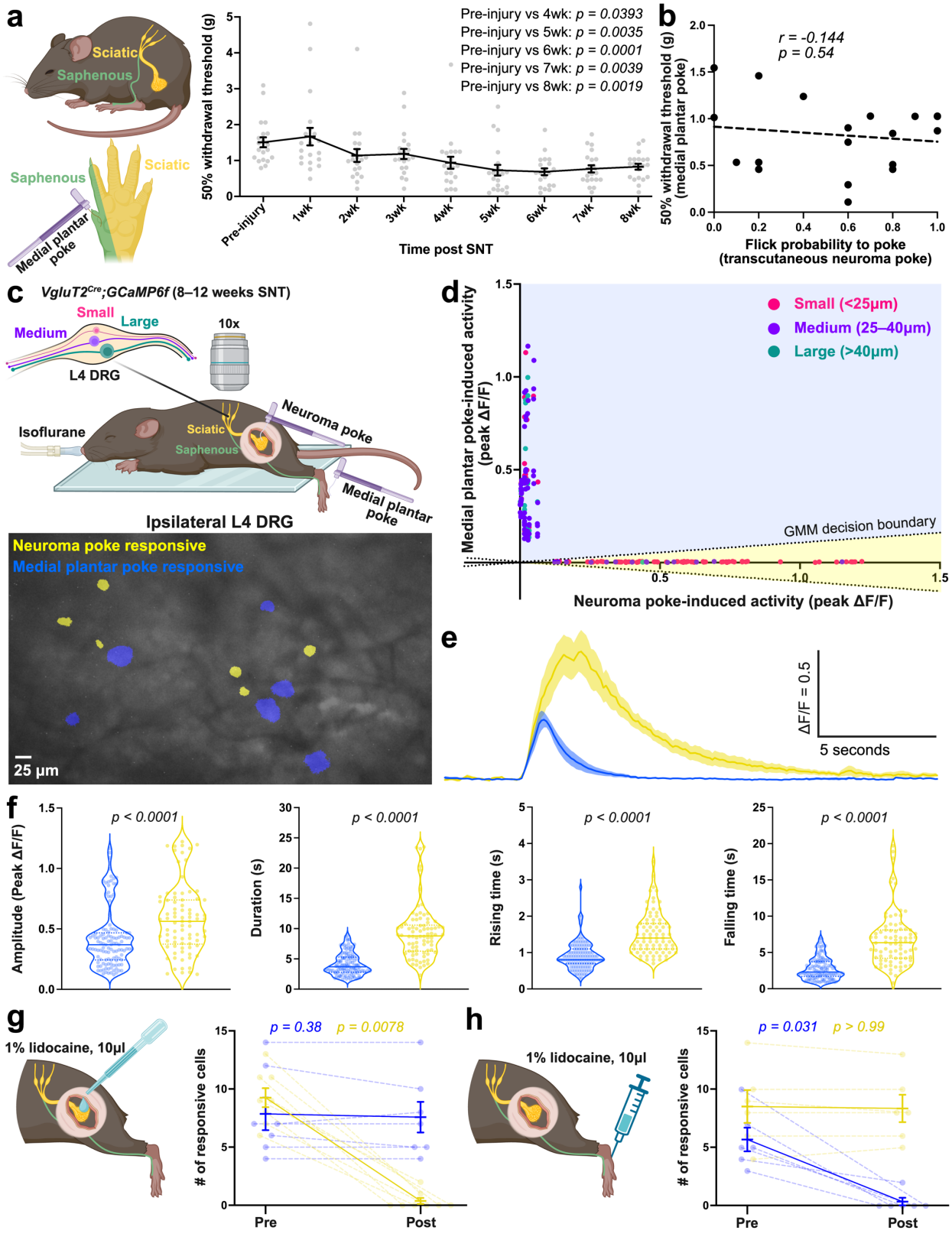
a
Sciatic
Saphenous
Saphenous
Sciatic
Medial plantar poke
50% withdrawal threshold (g)
Pre-injury vs 4wk: p = 0.0393
Pre-injury vs 5wk: p = 0.0035
Pre-injury vs 6wk: p = 0.0001
Pre-injury vs 7wk: p = 0.0039
Pre-injury vs 8wk: p = 0.0019
Pre-injury
1wk
2wk
3wk
4wk
5wk
6wk
7wk
8wk
Time post SNT
b
r = -0.144
p = 0.54
50% withdrawal threshold (g) (medial plantar poke)
Flick probability to poke (transcutaneous neuroma poke)
c
VglutT2Cre;GCaMP6f (8–12 weeks SNT)
Small
Medium
Large
L4 DRG
10x
Isoflurane
Sciatic
Saphenous
Neuroma poke
Medial plantar poke
Ipsilateral L4 DRG
Neuroma poke responsive
Medial plantar poke responsive
25 µm
d
Small (<25µm)
Medium (25–40µm)
Large (>40µm)
Medial plantar poke-induced activity (peak ΔF/F)
GMM decision boundary
Neuroma poke-induced activity (peak ΔF/F)
e
ΔF/F = 0.5
5 seconds
f
p < 0.0001
Amplitude (Peak ΔF/F)
Duration (s)
Rising time (s)
Falling time (s)
g
1% lidocaine, 10µl
p = 0.38
p = 0.0078
# of responsive cells
Pre
Post
h
1% lidocaine, 10µl
p = 0.031
p > 0.99
# of responsive cells
Pre
Post

1010

1011 **Fig. 3 | Distinct DRG neuron populations mediate pain from intact versus injured sensory fibres. a**,
1012 Schematic of the plantar von Frey assay targeting the medial plantar area innervated by the intact saphenous
1013 nerve (left) and quantification of the 50% withdrawal threshold (right). Each dot represents one mouse (n
1014 = 20). Data are mean ± SEM. *P* values from one-way ANOVA with Tukey's multiple comparisons. **b**,
1015 Pearson's correlation between the 50% withdrawal threshold from medial plantar poke and flick probability
1016 to transcutaneous neuroma poke at 8 weeks post-SNT. Each dot represents one mouse. **c**, Schematic of the
1017 *in vivo* L4 DRG calcium imaging setup for neuroma or medial plantar poke with a 1.4 g von Frey filament
1018 (top), and an example overlay showing cells responsive to neuroma poke and medial plantar poke (bottom).
1019 **d**, Classification of cells responsive to neuroma poke or medial plantar poke based on peak ΔF/F amplitude
1020 determined by GMM boundaries (dashed lines). Each dot represents one cell; no dual-responsive cells were
1021 observed. **e**, Calcium traces from neuroma poke-responsive (yellow) and medial plantar poke-responsive
1022 (blue) cells. Shaded bands indicate mean ± SEM from n = 5 mice (neuroma poke) and n = 4 mice (medial
1023 plantar poke). **f**, Quantification of response amplitude, duration, rising time, and falling time for each group.
1024 Each dot represents one cell. *P* values from two-sided Mann–Whitney tests. **g**,**h**, Number of cells responsive
1025 to a neuroma poke (yellow) or a medial plantar poke (blue) before and after topical lidocaine application to
1026 the neuroma (**g**) or intraplantar injection (**h**). Tests were performed 5 minutes after lidocaine administration.
1027 Data are mean ± SEM; dashed lines connect individual mice (n = 8 for neuroma application, n = 6 for
1028 medial plantar injection). *P* values from two-sided Wilcoxon matched-pairs signed-rank tests.

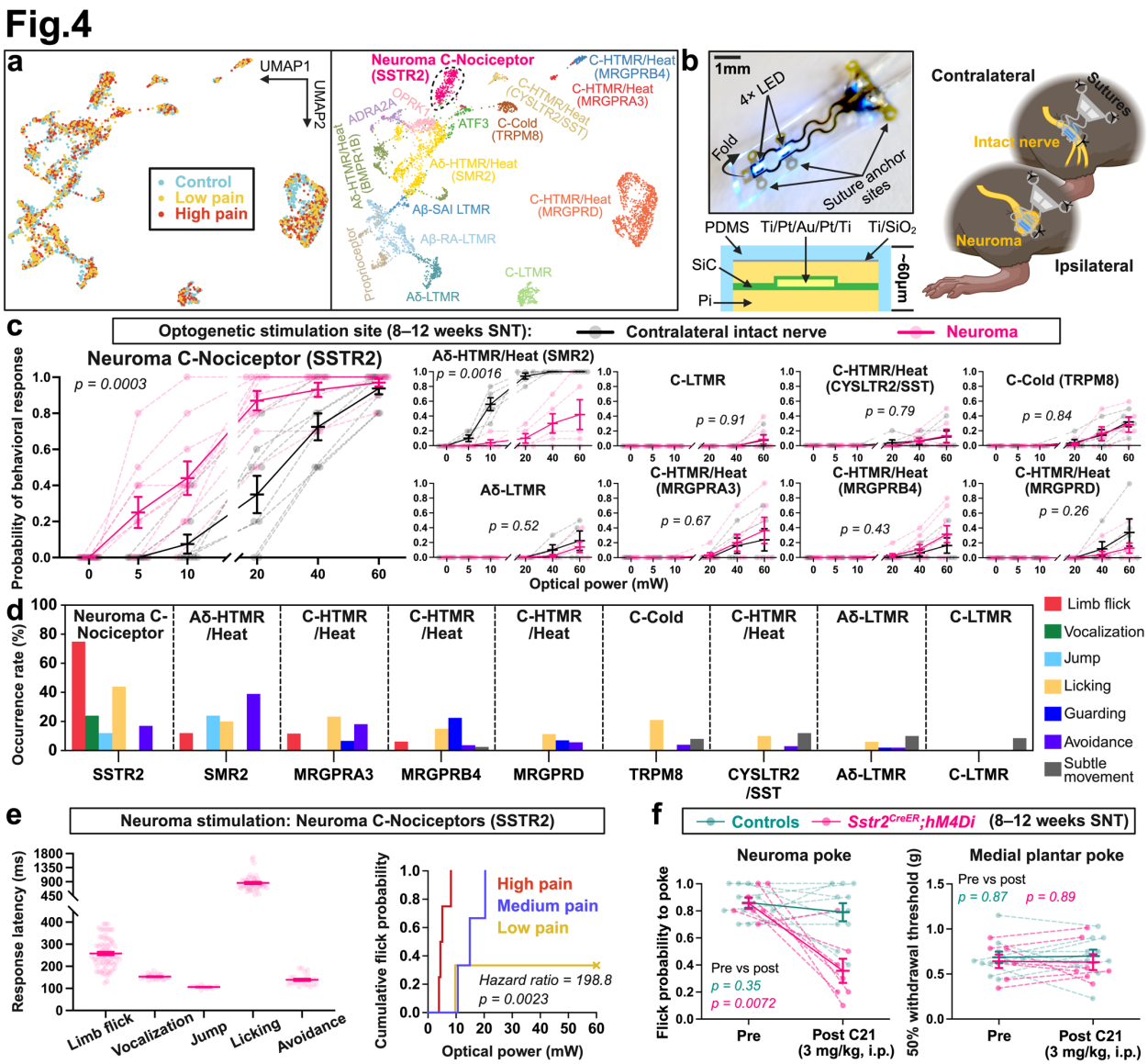

Fig. 4 | Neuroma C-Nociceptors (SSTR2) drive limb flicks. a, UMAP projections of DRG snRNA-seq showing nuclei from contralateral DRG (control), ipsilateral DRG from low-pain, and high-pain mice (left) and annotated sensory-neuron subtype identities (right). 10 weeks post-SNT mice were used for snRNA-seq. **b**, Photograph of the miniaturized blue LED cuff (top), schematic cross-section of the interconnects showing layered materials (bottom left; softness and flexibility were achieved by miniaturizing metal interconnects and incorporating soft polymer layers; see Extended Data Fig. 7 for details), and illustration of the implantation site for neuroma or intact sciatic nerve stimulation (right). **c**, Optogenetic activation of

1037 genetically defined neuronal subtypes (see Methods for the transgenic lines targeting each subtype). Optical
1038 power versus response probability for individual transgenic lines (10 trials per animal; single 10 ms pulse).
1039 Data are mean ± SEM; dashed lines connect individual mice. *P* values from two-way ANOVA with Tukey's
1040 multiple comparisons (figure shows the interaction effect of neuroma versus intact nerve stimulation across
1041 optical powers). **d**, Histograms showing the occurrence of different behaviours evoked at maximum optical
1042 neuroma stimulation (60 mW) using single 10-ms pulses. Note that multiple behaviours could occur in a
1043 single trial. **e**, Left: response latencies of individual behaviours relative to stimulus onset; data are mean ±
1044 SEM, each dot represents a single trial across n = 10 mice. Right: Cumulative flick probability (1 − Kaplan-
1045 Meier estimate) as a function of optical power for high-, medium-, and low-pain mice determined by
1046 transcutaneous neuroma poke. Cross mark at 60 mW indicates right-censoring for animals who did not
1047 show a flick at the maximum optical power. **f**, Limb flick probability to transcutaneous neuroma poke (left)
1048 and 50% withdrawal threshold from medial plantar poke before and after intraperitoneal (i.p.) injection of
1049 compound 21 (C21) in *Sstr2*^{CreER}*;hM4Di* mice (n = 7) for selective chemogenetic silencing of Neuroma C-
1050 Nociceptors (SSTR2) and littermate controls (*Sstr2*^{CreER} alone or *hM4Di* alone, n = 10). Data are mean ±
1051 SEM; dashed lines connect individual mice. *P* values from two-sided paired t-tests.

Extended Data Fig. 1

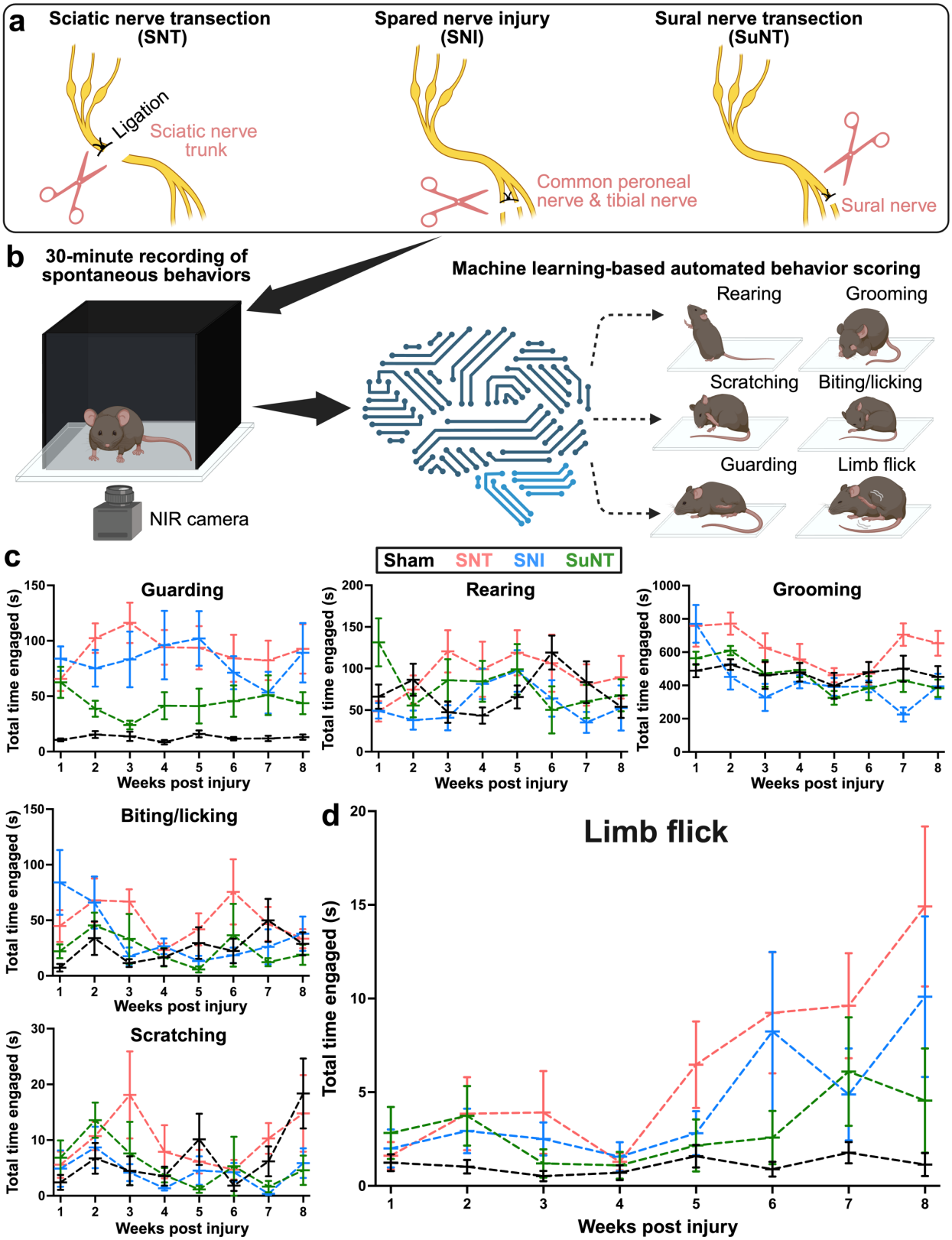

1052

1053 **Extended Data Fig. 1 | Automated behavioural screening reveals limb flick as a prominent behaviour**
1054 **in the chronic phase after peripheral nerve injury. a**, Schematics of three sciatic nerve injury models:
1055 sciatic nerve transection (SNT), spared nerve injury (SNI), and sural nerve transection (SuNT). **b**,
1056 Experimental setup for 30-minute recordings of spontaneous behaviours using a bottom-up near-infrared
1057 (NIR) camera and machine-learning–based automated scoring[18]. **c**,**d**, Total time spent on each indicated
1058 behaviour on the injured side, measured weekly for up to 8 weeks post-injury. Lines represent group means,
1059 error bars indicate ± SEM. For each injury type, n = 8 mice (4 males, 4 females).

Extended Data Fig. 2

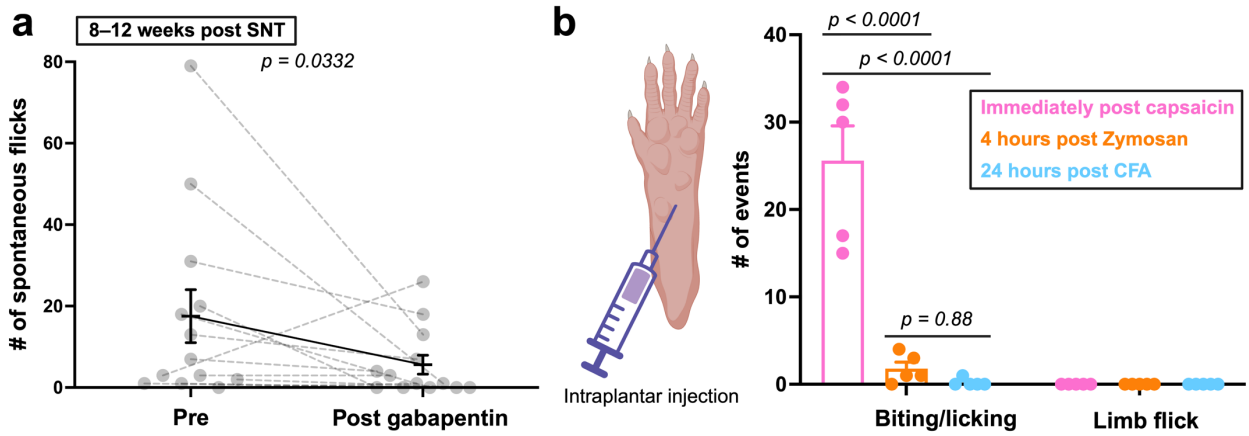

Extended Data Fig. 2 | Limb flicks are suppressed by gabapentin and are absent in acute pain conditions. a, Spontaneous limb flicks quantified over 30 minutes before and after intraperitoneal gabapentin (30 mg/kg) at 8–12 weeks post-SNT (n = 13 mice). Data are mean ± SEM; dashed lines connect individual mice. *P* value from two-sided Wilcoxon matched-pairs signed-rank test. **b**, Schematic of intraplantar injection (left) and quantification of biting/licking events and spontaneous limb flicks (right) following capsaicin (0.01%, 10 µL), Zymosan (100 µg in 10 µL), or complete Freund's adjuvant (CFA, 100%, 10 µL) injection. Behaviours were recorded for 30 minutes at peak-response windows defined from literature: immediately after capsaicin[18], 4 hours after Zymosan[53], and 24 hours after CFA[67]. Limb flicks are absent across all acute pain models, while biting and licking of the affected paw is the predominant behaviour in the capsaicin model. Each dot represents one mouse (n = 5 per model). Data are mean ± SEM; *P* values from one-way ANOVA with Tukey's multiple comparisons.

Extended Data Fig. 3

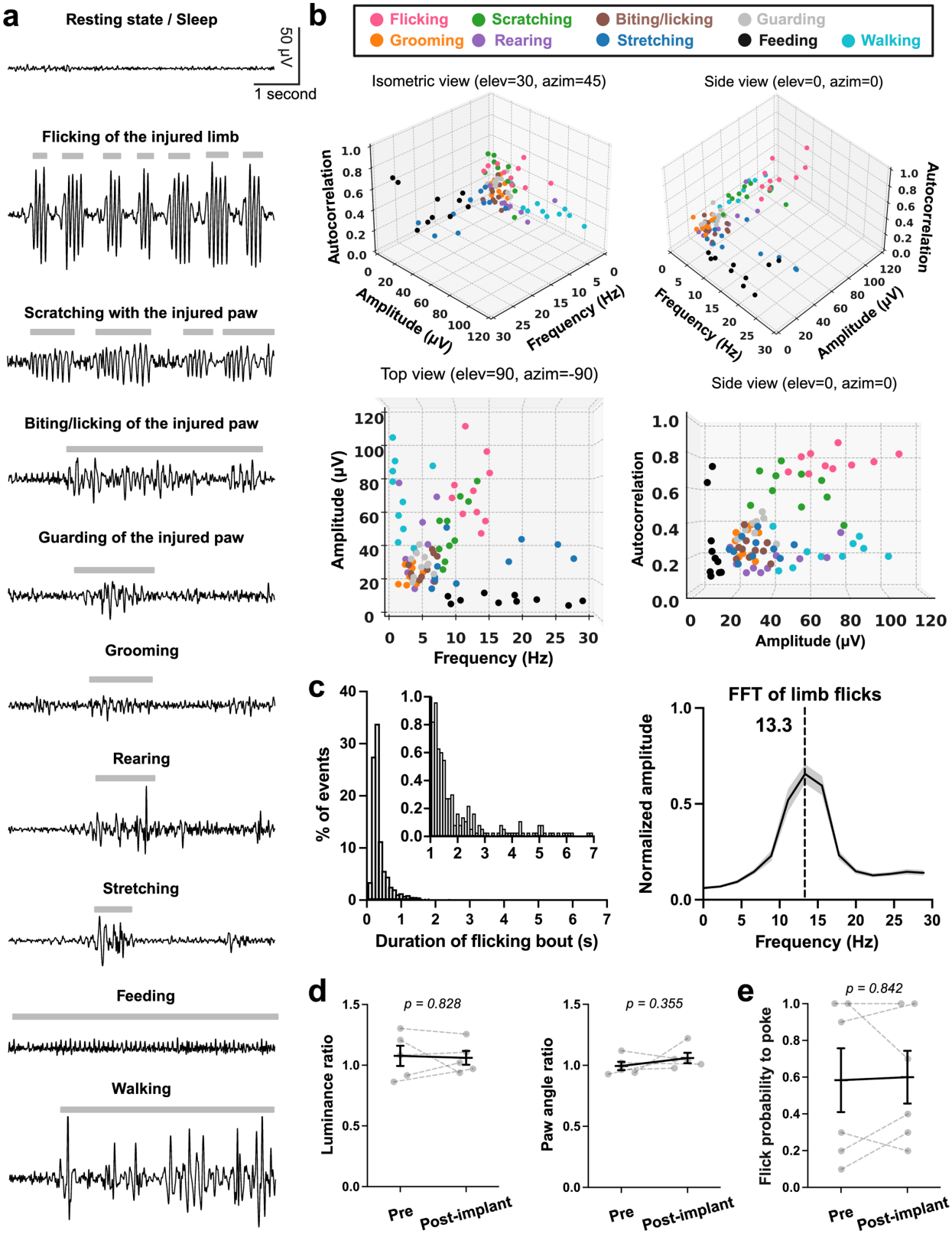

1071

1072 **Extended Data Fig. 3 | 24-hour EMG-based home-cage monitoring captures spontaneous limb flicks.**
1073 **a**, Representative EMG traces during various home-cage behaviours. Gray bars indicate periods when the
1074 behaviours occurred as confirmed by corresponding videos. **b**, Feature plots of peak amplitude, frequency,
1075 and autocorrelation coefficient (first non-zero positive peak) of EMG trace for each behaviour. Periodic
1076 movements such as limb flicks showed higher autocorrelation values. Each dot represents the average of
1077 20 events from one mouse (n = 10 mice, 12 weeks post-SNT). Elev, elevation; azim, azimuth. **c**, Left:
1078 histogram showing the duration distribution of individual limb flick bouts, with an inset expanding the 0–
1079 1% vs 1–7 seconds range. Most events occurred within 1 s. Right: Fast Fourier Transform (FFT) of limb
1080 flicks showing a dominant frequency at 13.3 Hz. **d**, Weight bearing and gait parameters measured by
1081 luminance ratio (left) and paw angle ratio (right)[53] before and two weeks after implantation of the wireless
1082 telemetry device without nerve injury (n = 5 mice). **e**, Flick probability to poke before and two weeks after
1083 implantation of the wireless EMG device (n = 6 mice at 8–10 weeks post-SNT). Data are mean ± SEM;
1084 dashed lines connect individual mice. *P* values from two-sided Wilcoxon matched-pairs signed-rank tests
1085 in (**d**,**e**).

Extended Data Fig. 4

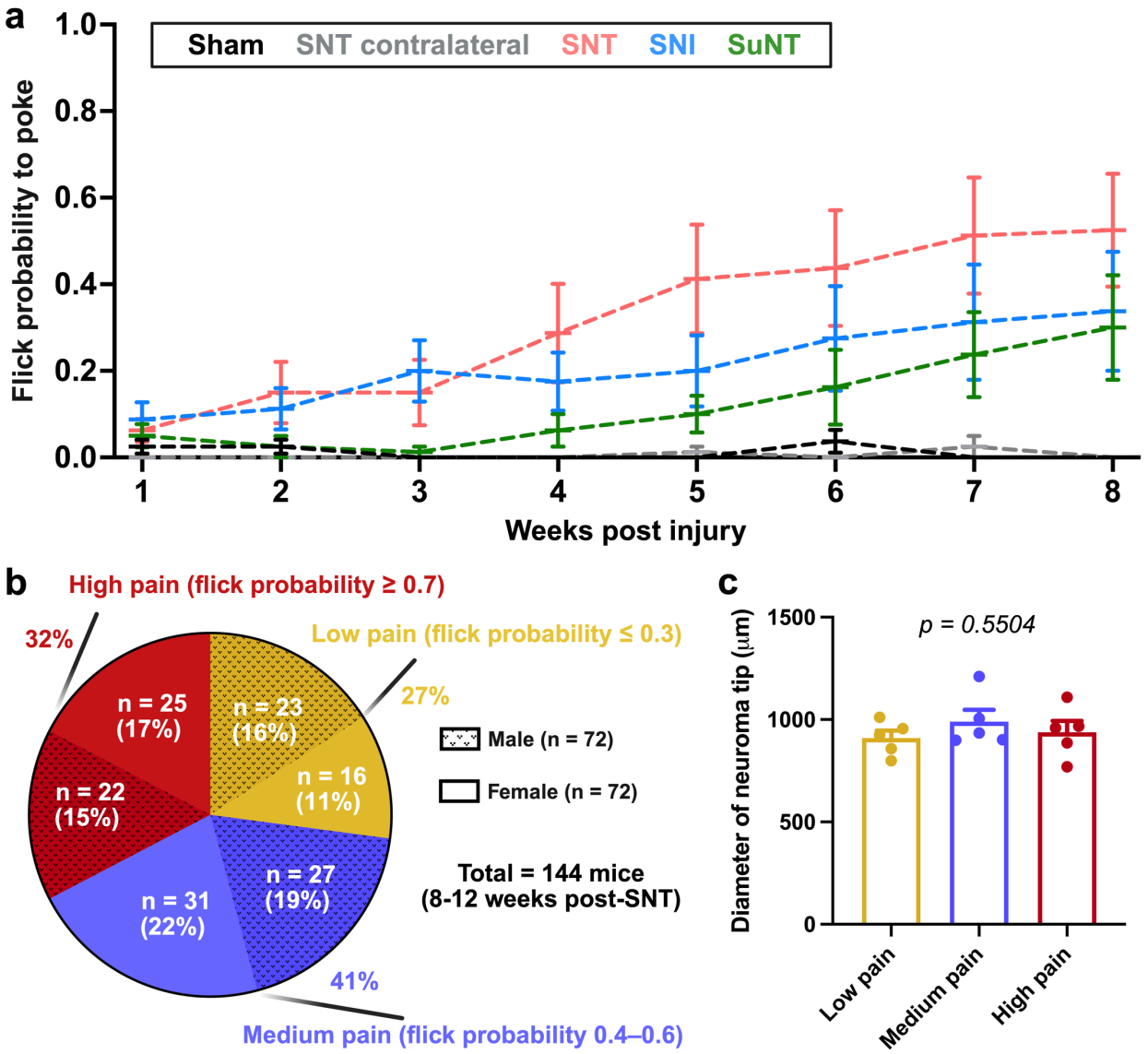

Extended Data Fig. 4 | Neuroma pain emerges across peripheral nerve injury models and shows differential pain severity. a, Flick probability in response to transcutaneous neuroma poke measured weekly for up to 8 weeks after injury. Lines represent group means; error bars indicate ± SEM. For each injury type, n = 8 mice (4 males and 4 females, as in Extended Data Fig. 1). **b**, Pie chart showing the distribution of high-pain, low-pain, and medium-pain phenotypes. **c**, Histogram showing the size of neuromas in each pain condition. Each dot represents a neuroma (n = 5 mice for each condition). *P* value from one-way ANOVA.

Extended Data Fig. 5

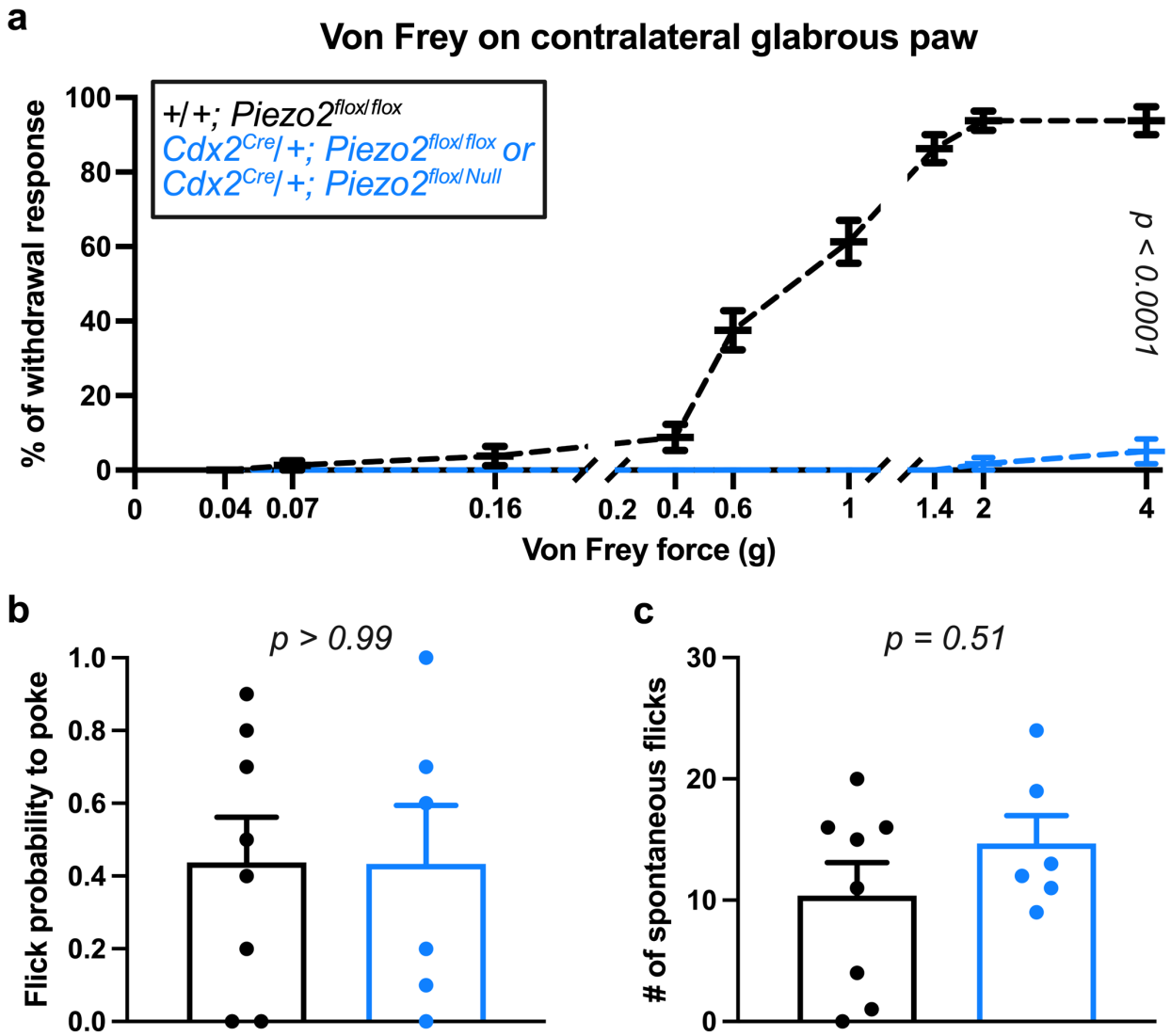

Extended Data Fig. 5 | Spontaneous limb flicks and flicks evoked by transcutaneous poke are independent of Piezo2. a-c, Von Frey filament evoked responses from contralateral glabrous paw (**a**), flick probability to transcutaneous neuroma poke (**b**), and spontaneous flick count over 30 minutes (**c**) at 8 weeks post-SNT in control and Piezo2 conditional knockout mediated by *Cdx2*^{Cre55}. Data are mean ± SEM; each dot represents one mouse (n = 8 controls, 6 knockouts). *P* values in (**a**) from two-way ANOVA with Tukey's multiple comparisons (figure shows the interaction effect of control vs knockout across von Frey forces), and from two-sided Mann–Whitney tests in (**b**,**c**).

Extended Data Fig. 6

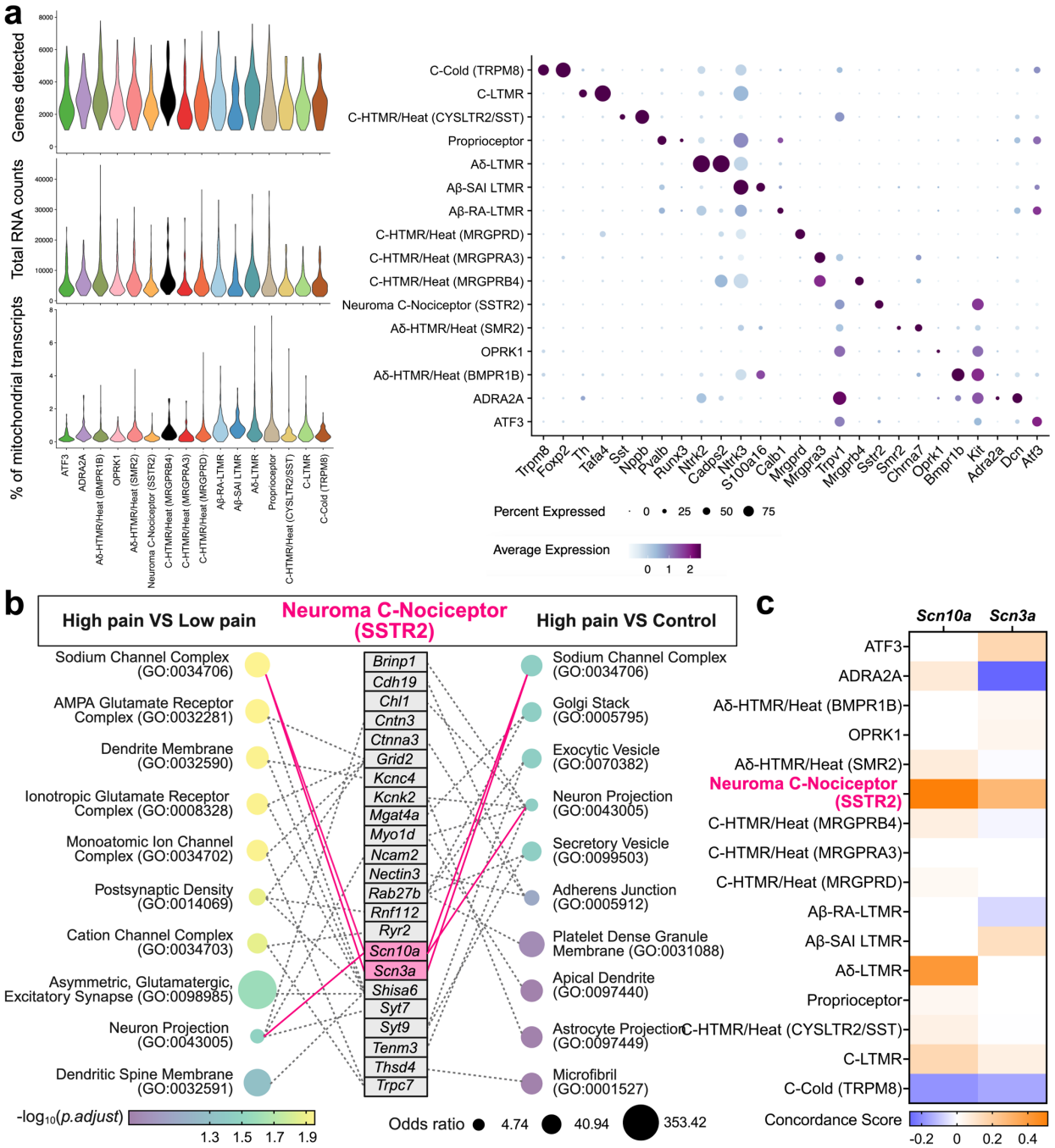

1100

1101 **Extended Data Fig. 6 | Transcriptomic profiling of DRG across pain conditions. a**, Violin plots showing
1102 quality control metrics, including the number of genes detected per nucleus (nFeature cutoff = 1,000), total
1103 RNA counts, and percentage of mitochondrial transcripts, and dot plots showing expression of canonical
1104 marker genes across neuronal populations. Dot size represents the percentage of nuclei expressing the gene,
1105 and dot colour reflects average expression level. Cell-type annotations follow previously described criteria[30].
1106 **b**, Gene Ontology enrichment within the Neuroma C-Nociceptor (SSTR2) population. Left: top 10 Cellular
1107 Component terms for high-pain vs. low-pain; right: top 10 Cellular Component terms for high-pain vs.
1108 control, ranked by adjusted *P* values. Middle column lists DEGs contributing to each term; solid magenta
1109 lines connect genes shared between contrasts, gray dashed lines connect genes appearing in only one
1110 contrast. **c**, Concordance scores for *Scn10a* and *Scn3a* across sensory neuron subtypes. The score is positive
1111 when a gene is up-regulated in both comparisons (high-pain vs. low-pain and high-pain vs. control),
1112 negative when down-regulated in both, and zero when regulation is inconsistent or observed in only one
1113 comparison; larger magnitude indicates stronger concordance (see Methods for formula).

Extended Data Fig. 7

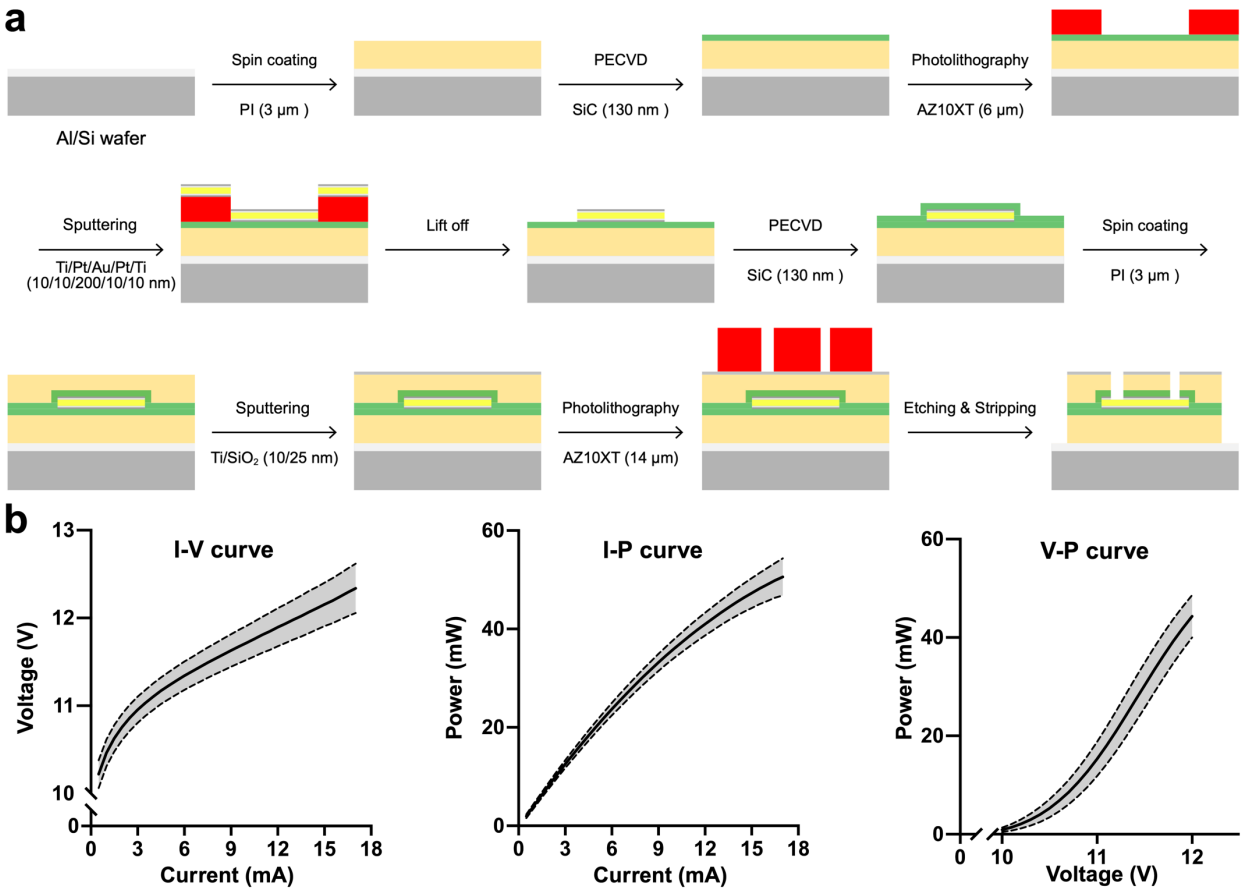

Extended Data Fig. 7 | Fabrication and characterization of the miniaturized LED cuff. a, Schematic of the fabrication process. A 3-μm polyimide (PI) layer is spin-coated onto an aluminum (Al)/silicon (Si) wafer, serving as a sacrificial substrate, and baked to complete imidization. A 130-nm silicon carbide (SiC) layer is deposited by plasma-enhanced chemical vapor deposition (PECVD). Metal interconnects consisting of Titanium/Platinum/Gold/Platinum/Titanium (Ti/Pt/Au/Pt/Ti) (10/10/200/10/10 nm) are sputtered and patterned by lift-off, followed by deposition of a second SiC layer and an additional PI layer. A Ti/SiO_2 bilayer (10/25 nm) is sputtered on the surface, and final device patterning is performed by inductively coupled plasma–reactive ion etching (ICP-RIE) to define cuff geometry and electrode windows. **b**, Electrical and optical performance of the integrated blue micro-LEDs (470 nm). Representative current–voltage (I–V), current–power (I–P), and voltage–power (V–P) curves. Solid lines and shaded bands represent mean ± SEM across n = 24 devices.

Extended Data Fig. 8

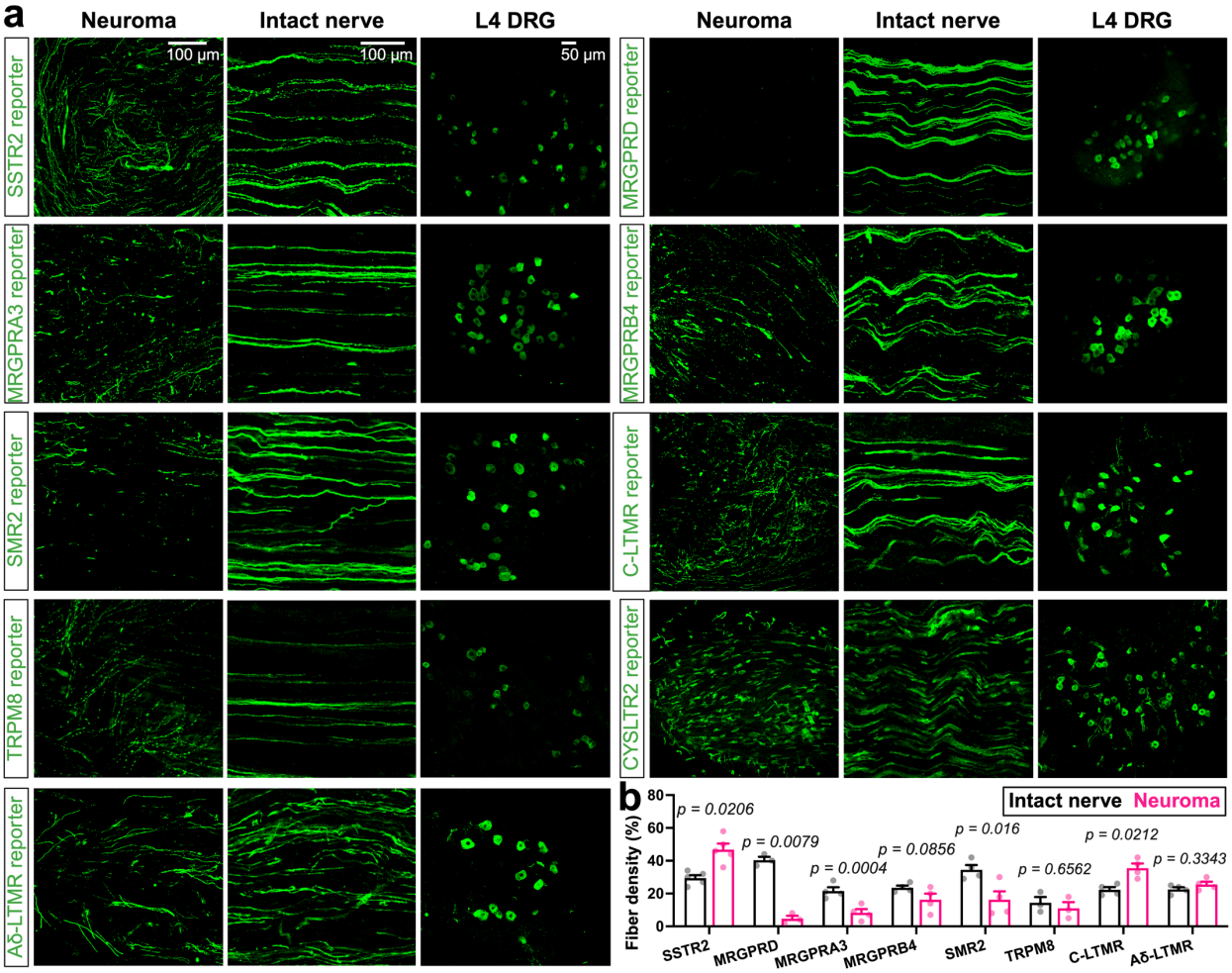

Extended Data Fig. 8 | Differential density of sensory fibre subtypes in neuromas. a, Representative images of reporter expression (ReaChR::mCitrine) in neuromas, contralateral intact nerves, and L4 DRG neurons from transgenic lines, including Neuroma C-Nociceptors (SSTR2), C-HTMR/Heat (MRGPRD), C-HTMR/Heat (MRGPRA3), C-HTMR/Heat (MRGPRB4), Aδ-HTMR/Heat (SMR2), C-Cold (TRPM8), C-LTMR, and Aδ-LTMRs. **b**, Quantification of fibre density, expressed as the percentage of axon-occupied area. Note that the increased density in neuromas labelled by the C-LTMR reporter may reflect contributions from both C-LTMRs and Th^{+} sympathetic nerves. C-HTMR/Heat (CYSLTR2/SST) fibres were not quantified because the transgenic line (*Cysltr2*^{Cre}) labels a mixture of axons and non-neuronal cells in peripheral nerves. Data are mean ± SEM; each dot represents one nerve/neuroma. *P* values from two-sided

1135 paired t-tests are shown for each population. All these histology studies were performed following the

1136 optogenetic activation experiments at 8–12 weeks post-SNT.

Extended Data Fig. 9

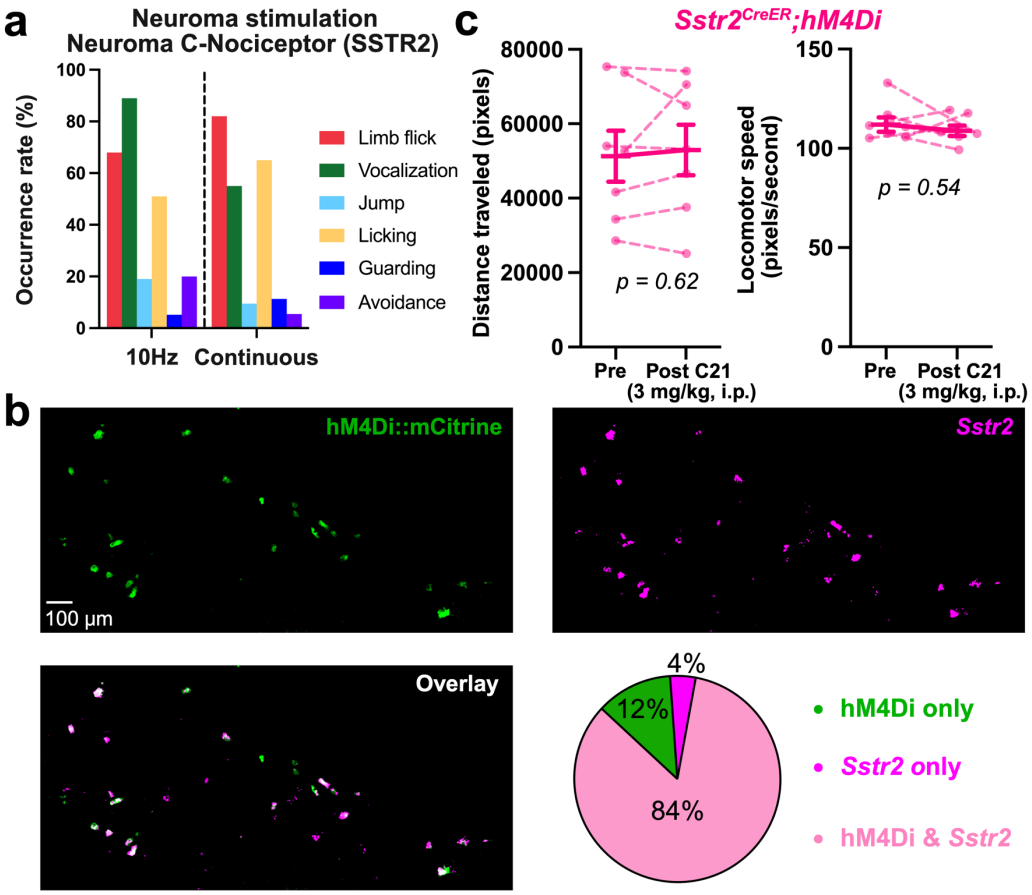

Extended Data Fig. 9 | Gain- and loss-of-function analyses of Neuroma C-Nociceptors (SSTR2). a, Occurrence of behaviours in response to a 5-s stimulation, delivered either as a 10 Hz train of 10-ms pulses or as continuous light. **b**, Representative images and quantification of combined *in situ* hybridization for *Sstr2* and immunolabeling of hM4Di::mCitrine in the ipsilateral L4 DRG of *Sstr2*$^{T2a\text{-}CreER}$; *R26*$^{LSL\text{-}hM4Di::mCitrine}$ mice. Twenty L4 DRG sections from two *Sstr2*$^{T2a\text{-}CreER}$; *R26*$^{LSL\text{-}hM4Di::mCitrine}$ mice were used to quantify the overlap ratio between *Sstr2* mRNA and hM4Di::mCitrine expression. **c**, Quantification of distance traveled and locomotor speed before and after acute chemogenetic silencing using a previously reported behavioural platform[53]. Data are mean ± SEM; each dot represents one mouse (n = 7 mice). *P* values from two-sided paired t-tests.